

Accurate X-ray Absorption Spectra of Dilute Systems: Absolute Measurements and Structural Analysis of Ferrocene and Decamethylferrocene

M. T. Islam,[†] S. P. Best,[‡] J. D. Bourke,[†] L. J. Tantau,[†] C. Q. Tran,[¶] F. Wang,[§] and C. T. Chantler^{*,†}

[†]School of Physics, University of Melbourne, Parkville, Vic 3010, Australia

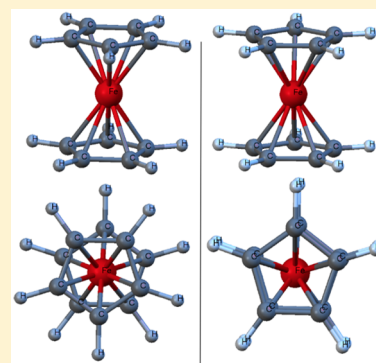
[‡]School of Chemistry, University of Melbourne, Parkville, Vic 3010, Australia

[¶]School of Physics, La Trobe University, Melbourne, Vic 3086, Australia

[§]Department of Chemistry and Biotechnology, Swinburne University of Technology, Melbourne, Vic 3122, Australia

Supporting Information

ABSTRACT: X-ray absorption fine structure (XAFS) of ferrocene (Fc) and Decamethylferrocene (DmFc) have been determined on an absolute scale using transmission measurements of multiple solutions of differing concentrations (15 mM, 3 mM, pure solvent) at operating temperatures of 10–20 K. Mass attenuation coefficients and photoelectric absorption cross sections are measured and tabulated for both molecules for an extended energy range in excess of 1.5 keV from the Fe K-shell absorption edge. At these temperatures, the minimization of dynamic disorder has enabled a critical determination of the oscillatory absorption structures created by multiple-scattering paths of the excited photoelectron. These oscillatory structures are highly sensitive to the local conformation environment of the iron absorber in organometallic structures. Crystallographic and scattering studies have reported both structures characterized by staggered cyclopentadienyl rings, in contrast with low temperature crystallography and recent density functional theoretical predictions. Phase changes in the crystallographic space groups are reported for Fc at different temperatures, raising the possibility of alternative conformation states. Robust experimental techniques are described which have allowed the measurement of XAFS spectra of dilute systems by transmission at accuracies ranging from 0.2% to 2%, and observe statistically significant fine structure at photoelectron wavenumbers extending to $>12 \text{ \AA}^{-1}$. The subtle signatures of the conformations are then investigated via extensive analysis of the XAFS spectra using the full multiple scattering theory as implemented by the FEFF package. Results indicate a near-eclipsed D_{5h} geometry for low-temperature Fc, in contrast with a staggered D_{5d} geometry observed for DmFc. The ability of this experimental approach and data analysis methodology combined with advanced theory to investigate and observe such subtle conformational differences using XAFS is a powerful tool for future challenges and widens the capacity of advanced XAFS to solve a broad range of challenging systems.



1. INTRODUCTION

As suggested by Seeman and Cantrill¹ in their recent *Nature Chemistry* commentary, X-ray measurement has been the most important structure characterization technique for an unknown compound in history. X-ray absorption fine structure (XAFS) refers to the complex oscillatory structure that is typically seen in an X-ray absorption spectrum at energies just above an ionization edge, and is created by the backscattering and self-interference of the excited photoelectron. XAFS is therefore a spectroscopic technique that uses X-rays to probe the structure of matter at an atomic scale; it is element-specific, since X-rays are tuned to be at and above the binding energy of a particular core electronic level of a particular atomic species. As a result, XAFS is a powerful technique for elucidating the local molecular structures by modeling of the various chemical, electronic, and thermodynamic material properties. XAFS is currently one of the most prolific applications of synchrotron radiation,² due to its versatility in probing the local environment of the absorbing atom which can be in any phase of matter. XAFS has provided quantitative insights in

many fields including material science, transition metal chemistry, metal catalysts, environmental science, and biological science.^{3–5} There is a vast swathe of papers using XAFS on organometallic compounds. This has recently yielded significant structural insights into the environment of coordination complexes.⁶

Notwithstanding these significant successes of XAFS, the detail and reliability of structural information obtained from XAFS is often limited due to the relative nature of many standard measurements, poor characterization of experimental uncertainties, and ill-defined refinement statistics from standard theoretical approaches.⁷ High absolute accuracy modern measurements such as those using the X-ray extended range technique (XERT)⁸ have shown success in quantifying XAFS spectra with uncertainties less than 0.1%. However, such measurements have typically been limited to less complex systems such as metallic foils.^{9,10}

Received: January 15, 2016

Revised: April 14, 2016

Given the sensitivity of XAFS to elucidate variations in molecular structures, co-ordination geometry and chemical properties, it is critical that similarly accurate methodologies are developed for use in less ideal systems such as complex molecules and dilute systems in order to unlock the full analytical potential of this technique. Recent work has demonstrated success in applying many of the features of the XERT to dilute solutions containing Ni complexes using the hybrid technique for XAFS.¹¹

Ferrocene (Fc) represents large and significant challenges in its structural characterization in the history of chemistry as indicated by the recent “wrong but seminal” discussion.¹ Fc is one of the most studied organometallic systems. New development of the understanding of Fc is generally of broad interest and significance since it provides a high symmetry molecule with long-range interactions between the Cp ligands which are counterbalanced by metal-arene interactions. Fc and Decamethylferrocene (DmFc), their extended structures, and derivatives have been adopted for various applications in catalysis, fuel additives, and pharmaceuticals, since the discovery of Fc in 1951.¹² In particular, the stability of these compounds is highly dependent on their local electronic structures, and hence conformation. Although long accepted to both possess dual pentagonal carbon rings with a staggered or D_{5d} symmetry,¹³ it has been suggested theoretically for Fc that an eclipsed or D_{5h} symmetry should be more stable by up to 4 kJ mol⁻¹.^{14–16} Such an eclipsed conformer has not been verified experimentally in a robust and definitive manner, though some evidence has been presented to that effect. Temperature-dependent diffraction studies have suggested that crystalline Fc undergoes a phase transition at 164 K,¹⁷ where the monoclinic high temperature phase is disordered^{18,19} and transformed into a triclinic crystal, for temperatures at least down to 101 K.¹³ This appears to be associated with a conformational change characterized by a relative rotation of the carbon rings. As a result, this becomes the target of the present XAFS study for Fc.

No conformational change is expected for DmFc due to the greater steric hindrance, and therefore a comparison between Fc and DmFc at low temperatures is warranted. For this reason, we employ XAFS spectroscopy to study Fc and DmFc conformers, in order to establish a direct probe of molecular structure, applicable to dilute and disordered systems. In order to avoid intermolecular interactions such as crystal packing etc. which may confuse the conformer information, the XAFS measurements were performed in a dilute system rather than in a crystal form. For the Fc and DmFc samples studied, the XAFS is able to probe an effectively isolated molecule with natural structural and thermal disorder.

Identification of rotamers of sandwich compounds such as ferrocene presents one of the most technical challenges for XAFS spectroscopy. In fact, none of the existing measurements/techniques studying ferrocene is able to lead information which conclusively identifies the conformers of this difficult example. This is also a challenge to theoretical studies. As a result, a search for appropriate properties and techniques which are unique signatures for the Fc conformers becomes an important task. In the present study, the XAFS spectroscopy combined with theoretical study are employed to explore conformer specific information on ferrocene.

In this manuscript, we present:

The first absolute accurate XAS measurements of ferrocene, using new techniques and the new XAS hybrid approach; one of the first absolute accurate XAS measurements of a dilute system or solution; the first structural analysis properly accounting for

experimental uncertainty for ferrocene XAS; significant evidence to discriminate subtle structural and conformational difference contributing only a few percent of the (dilute) XAFS signal and relating to multiple distant paths only; and one of the first two structural analyses using experimental uncertainty for XAS of any dilute system or solution (1–15 mM).

It is common for XAS structural analysis for dilute solutions to use fluorescence XAS. However, here we present techniques for transmission XAS which can be more accurate and more insightful than fluorescence measurements, with fewer unknown errors, even for dilute solutions. The use of 10–20 K makes the measurement more sensitive or insightful. Two key markers presented in the abstract are the defined accuracies to 0.2% and the sensitivity of k -ranges to $>12 \text{ \AA}^{-1}$, a record for this type of measurement in transmission at low concentrations. These new techniques are able to be sensitive discriminants of such subtle difference signatures, which argues for a broader and wider application to other complex or impenetrable problems across fields arising for numerous other solutions, frozen or at room temperature.

2. OUTLINE WITH SIGNIFICANCE

This manuscript develops the use of the hybrid technique to measure high-quality XAFS data for a nonideal system in transmission, applies the method to iron-containing organometallics, and provides spectroscopic evidence for the conformation geometries of the Fc and DmFc molecules in isolation at low temperatures.

Section 3, Experimental Methods: The Hybrid Technique for Dilute Systems, introduces key aspects of the novel hybrid technique as applied at ANBF, Tsukuba, Japan, and in this experiment as applied to dilute solutions (15–3 mM Fc, DmFc). **Sample details and measurement** are presented.

Section 4, Determining Attenuation Using the Hybrid Technique for Multiple Dilute Solutions, presents the early reproducibility and precision of the 15 mM and 3 mM solutions and of the solvent or blank XAFS by transmission, showing that high reproducibility (to 0.01%) including several systematic sources of noise can be obtained on a low-flux, low-brightness source with careful setup and measurement. We then discuss new approaches to **normalization to solvent** of the sample measurements, as some key systematics are clearly larger than the reproducibility measures. This involves presenting and explaining the key equations for processing and propagating measurement uncertainties from multiple readings. Associated with the critical uncertainty of the **determination of path length** for multiple cells of frozen solutions, this then permits the isolation of contributions to the background. It is particularly impressive that these featureless curves are not parallel and that the energy dependence allows one to distinguish separate contributions of each background component to the experimentally measured spectra. Having achieved this, we discuss the new methodology for **extraction of attenuation of the active species in the sample** and thereby extract the normalized XAFS with uncertainties propagated from the analysis. Perhaps particularly exciting is the separation of distinct uncertainty contributions to the spectrum from different sources and that the total is of order $0.0002 \text{ in } \left[\frac{\mu}{\rho} \right] [\rho t]$ for the samples.

Section 5, Characterization of Experimental Systematics for Their Correction, Dependent upon Beamline, briefly discusses how the analytical methodology measures and observes **energy calibration, scattering, and harmonic contamination** and

assesses any systematic corrections to the data needed from these sources.

A key result for accurate measurement is presented in section 6, X-ray Mass Attenuation Coefficients of Compounds from Dilute Solutions, providing normalized extracted mass attenuation coefficients with absolute and relative uncertainties. Tabulations of these with uncertainties are presented in Supporting Information. Accuracies of 0.1% to 1% resulted from this analysis for such dilute systems, by transmission XAFS using the Hybrid technique.

The section Extraction of Oscillatory Spectral Structures for Conformational Analysis is critical to the following discussion of structural parameters. While there are numerous conventional ways of preparing such extracted $k^2\chi$ vs k plots for structural analysis, this analysis is unique in presenting explicit uncertainties associated with this process. We omit direct evaluation of the impact of assumptions and uncertainties of the E_0 fitting and k -weighting, or the functional forms of the spline removal—we discuss these in other publications.

Section 7, Theory and Analysis of Experimental Data, initially reviews prototype structures from experiment in order to investigate the applicability of (usually room temperature crystallography) structure for Fc to those for dilute or isolated molecular Fc toward 10 K. The analysis and investigation of reported Fc structures enables us to answer questions including: Which literature structure most closely approximates the current experimental data? What limitations are there due to crystal forces or thermal disorder? Do these conclusions pertain after regularization to reflect the symmetry of the molecule rather than the space group of a crystal? This section concludes with conformational analysis of Fc and sensitivity of ring rotation, which proves the extreme subtlety of the question of molecular symmetry in dilute solutions, and the complexity of error analysis required to observe a difference signature in the FEFF/muffin-tin theoretical environment. Inclusion of variation of thermal parameter refinement allows conclusions to be made in relation to the utility of a priori crystal structures versus direct experimental data from advanced XAFS.

Following this, section 8 XAFS Refinement Using Structural Models from DFT. Insight from the Hybrid Technique, then presents the preference and suggestive evidence for the eclipsed conformation for Fc and the preference and suggestive evidence for CCSD(T) DFT theoretical model versus alternate DFT modeling. In some sense, this is a core conclusion, but to confirm the validity of the result, we proceed to study DmFc.

Section 9, Refinement of DmFc Conformations and Consistency, similarly asks for DmFc: Which literature structure most closely approximates the current experimental data? What limitations are there due to crystal forces or thermal disorder? Do these conclusions pertain after regularization to reflect the symmetry of the molecule rather than the space group of a crystal? Finally, the study observes the preference and suggestive evidence for the staggered conformation for DmFc, which thereby, by contrast, provides the key evidence for the eclipsed conformation of Fc.

3. EXPERIMENTAL METHODS: THE HYBRID TECHNIQUE FOR DILUTE SYSTEMS

This work uses an implementation of the hybrid technique to measure high absolute accuracy XAFS of low-temperature dilute solutions containing the organometallics ferrocene (Fc, $\text{Fe}(\text{C}_5\text{H}_5)_2$) and Decamethylferrocene (DmFc, $\text{Fe}(\text{C}_5(\text{CH}_3)_5)_2$). The range of measured energies covers in excess of 1.5 keV from the K-shell

ionization edge of Fe for all data sets, enabling a detailed study of the XAFS structure of the active metallic centers, and a robust extended-range absorption calibration to accurately quantify the data on an absolute scale.

Samples of Fc, DmFc, and the solvents butyronitrile ($\text{CH}_3\text{CH}_2\text{CH}_2\text{CN}$) and acetonitrile (CH_3CN) were obtained from commercial sources (Aldrich) and were used as received. The solvent was prepared using 50% butyronitrile ($\text{CH}_3\text{CH}_2\text{CH}_2\text{CN}$) and 50% acetonitrile (CH_3CN), the mixed solvent being less susceptible to crystallization during freezing.

X-ray absorption measurements were performed at the Australian National Beamline Facility (ANBF) in Tsukuba, Japan, utilizing the established experimental geometry of the hybrid technique (Figure 1).²⁰ Multiple solutions with differing concentrations for each of the compounds—Fc and DmFc—as well as a mixed solvent, identical to that used to prepare the solutions, were loaded into the sample compartments of a multichambered solution cell, loaded into the beamline within a cryostat,¹¹ operating at base temperature (10–20 K). Data were collected in two runs at each of three sample positions to provide measurements from Fc (3.07 mM, 15.26 mM) and DmFc (3.06 and 15.29 mM) together with solvent and air path. Measurements of the mixed solvent and empty cell allows quantification of attenuation from the sample holders, air path, and other static experimental components. In addition to the dilute samples within the cryostat, a 10 μm thick metallic iron foil was used for secondary absorption measurements at room temperature.

Photon flux was measured using three ion chambers as shown in Figure 1. At each energy, measurements were repeated 7–10 times to ensure sufficient counting statistics and accurate data collection. The X-ray beam was monochromated via a detuned silicon double-crystal Bragg monochromator, and its primary energy was calibrated using the BigDiff powder diffractometer.²¹ Potential harmonic contamination of the beam was detected via the use of two daisy wheels positioned upstream and downstream in the X-ray beam.²²

Sample Details and Measurement Conditions at Cryogenic Temperatures. Solutions were loaded into the sample compartments of the solution cell following a constant-flow mechanism established as part of the hybrid technique,²⁰ and frozen by immersion into liquid nitrogen.

As the effective path length $[\rho t]$ of a given solution is changed significantly at low temperature (10–20 K), accurate measurements of sample properties, and in particular the density of the frozen solution, were important to isolate the solvent effects from the solution attenuation. Since the path length of the solution is not accurately known, owing to the flexibility of the Kapton windows, the density of the solvent allowed the determination of the path length $[\rho t]_{\text{sv}}$ of the pure solvent and other frozen solutions.

4. DETERMINING ATTENUATION USING THE HYBRID TECHNIQUE FOR MULTIPLE DILUTE SOLUTIONS

Nominal transmission intensities (I_0 , I_1) for each solution, the pure solvent, blank measurements, and dark-current measurements were used to determine the absolute X-ray attenuations of Fc and DmFc. Removal of the effect of dark current in the measured intensities uses a linear function to fit the recorded dark currents in monitor and detector aggregated over time. This measurement also enables a quantification of the contribution of uncertainties in dark current to the total attenuation. Figure 2 gives the dark-current corrected attenuations for Fc, in addition to the associated percentage uncertainties for each concentration.²³

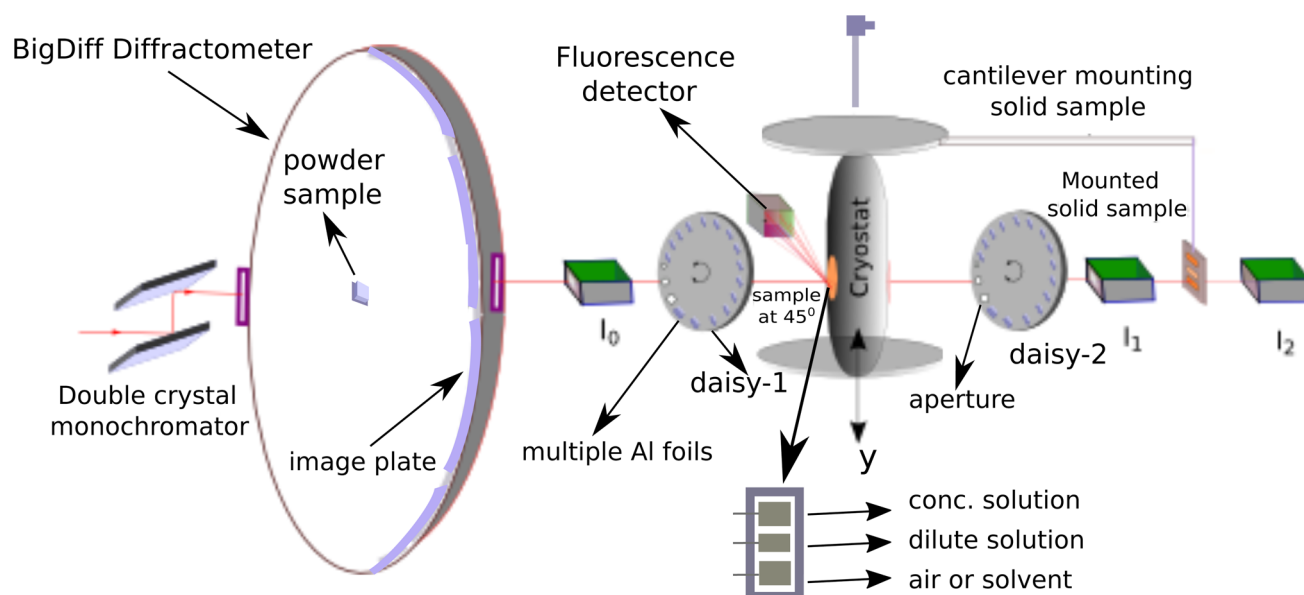


Figure 1. Schematic diagram of the hybrid technique²⁰ experimental setup at ANBF, Tsukuba, Japan, for intensity measurements using multiple solutions of ferrocene and decamethylferrocene. Measurements were made using a multichambered solution cell in the cryostat at temperatures from 10 to 20 K. The cryostat required vertical translation for each energy to access each of the samples. Two daisy wheels containing 14 aluminum filters (of different thicknesses) were employed upstream and downstream to monitor harmonic contents, while three further apertures of varying size on each wheel allowed for monitoring of direct scattering contributions. In addition to measurements in transmission mode, a multielement detector was positioned for simultaneous measurements of fluorescent scattering intensities.

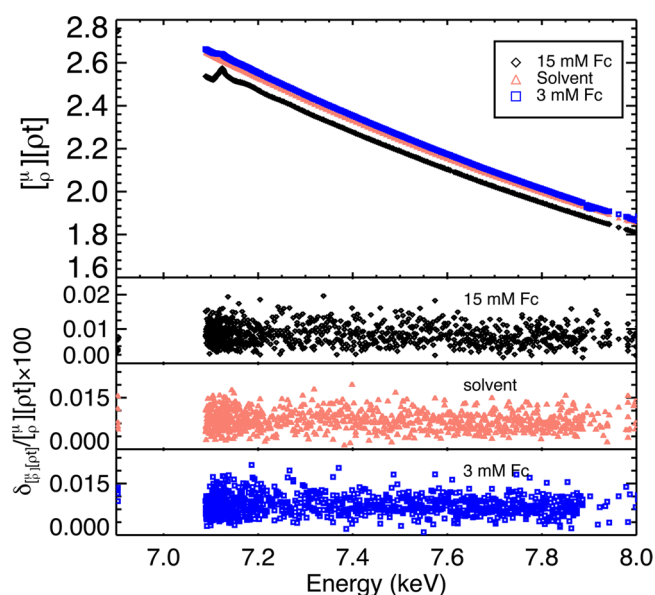


Figure 2. Attenuations of the 15 mM and 3 mM solutions of Fc, and of the pure solvent, represented respectively by black diamonds, blue squares, and red triangle markers. The uncertainties determined from repeated measurements from 0.005% to 0.02% reflect the high quality of the data. Well-defined peaks from the 15 mM solution, relatively weak peaks from the 3 mM, and no peaks from the pure solvent confirmed there was no cross-contamination leaking between the chambers (following the cell design). The solutions were confined to three chambers, each of 1.5 mm nominal path length.

These uncertainties are extremely small, and predictably quite similar for each concentration. They are therefore not significant contributors to the final uncertainty of these measurements.

The 15 mM solution exhibits relatively well-defined peaks, while the 3 mM solution exhibits a weaker structure, and no structure is visible for the solvent. The blank measurement allows

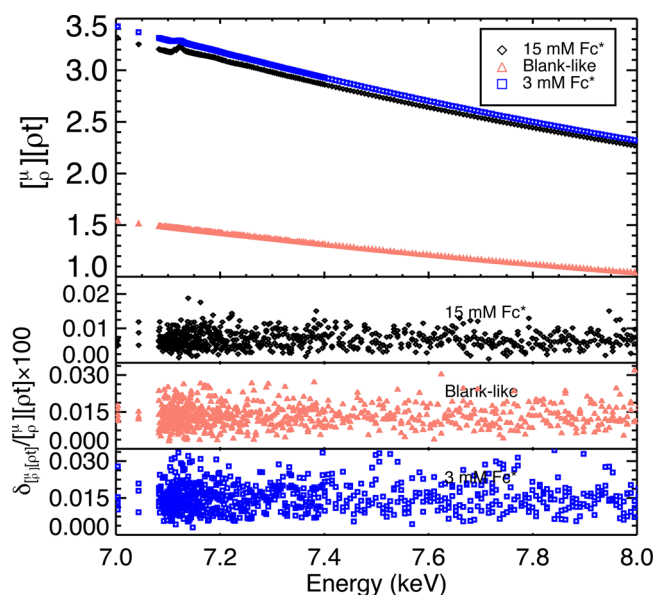


Figure 3. Attenuation from the 15 mM and 3 mM DmFc solutions, denoted Fc*, and of a blank measurement using an empty chamber are represented respectively by black diamond markers, blue squares, and salmon triangles. The uncertainties determined from the repeated measurements varied from 0.005% to 0.03% representing the high quality of the data. The blank sample produced a smooth curve with substantially less attenuation, contributed primarily by components such as the sample holder, cryostat, detector windows, and air path.

a confirmation of the integrity of the samples in the multisample holder.

Corresponding measurements for DmFc are shown in Figure 3. In this case the attenuation represented by the salmon colored Δ markers is only for the background signal because there was no sample (i.e., an empty chamber was used) in the path of the beam, and thus there is very little attenuation.

Table 1. Estimated Attenuation Contributions by the Background Absorbers Using FFAST Theoretical Data of X-ray Mass Attenuation Coefficients and Geometry of the Experimental Setup

background absorber	chemical formula	density (g/cm ³)	path length (cm)	$[\rho t]_{av}$ (g/cm ²)
air	N ₂ (78%) + O ₂ (21%) + Ar(0.93%)	0.0011	39.8 ± 0.7	0.0430
silicone	CH ₃ Si ₂ O ₂ C ₄ H ₉	0.968	0.03	0.0290
Kapton	C ₁₂ H ₁₀ N ₂ O ₅	1.15	0.02	0.0230
detector gas	N ₂	0.0012	19.0 ± 0.2	0.0228
cryostat gas	He	0.000 18	2.2	0.0004

Normalization of Attenuation to Solvent: Determining Attenuations of the Solutes. Attenuation of solutions are affected by significant background absorption and scattering contributed by the solvent and other experimental components such as the detector gas, air path, Kapton or beryllium windows, sample holders etc. positioned between the monitor and the detector. When the solution is sufficiently dilute, these background signals can be much larger than the signal for the solute (substance in solution). The attenuation of the solute can be determined by separating the solvent contributions:

$$\left[\frac{\mu}{\rho}\right][\rho t]_S = \left[\frac{\mu}{\rho}\right][\rho t]_{S+SV+BG} - \left[\frac{\mu}{\rho}\right][\rho t]_{SV+BG} \quad (1)$$

which may also be expressed directly in terms of incident and transmitted intensities:

$$\left[\frac{\mu}{\rho}\right][\rho t]_S = -\ln\left(\frac{I - I_d}{I_0 - I_{d0}}\right)_S + \frac{t_S}{t_{SV}} \ln\left(\frac{I - I_d}{I_0 - I_{d0}}\right)_{SV} + \ln\left(\frac{I - I_d}{I_0 - I_{d0}}\right)_{BG} \quad (2)$$

where the subscripts *S*, *SV*, *BG* refer to the solute, solvent, and other background absorbers, respectively. The factor of $\frac{t_S}{t_{SV}}$ represents the ratio of the thickness of the solution to the pure solute, as measured directly for *Fc*. I_0 and I_1 are the nominal intensities before and after attenuation by the sample, and I_{d0} and I_d are dark-currents measured by the same ion chambers in the absence of the X-ray beam. Although the nominal thicknesses of the chambers used for these measurements is the same, small variations of this parameter from unity may lead to significant errors due to the majority contribution of the solvent to the total attenuation.

Assuming that the solvent measurements were uncorrelated with the solution measurement, and including the correction for solvent path length, the uncertainty in the attenuation of the solute may be expressed in terms of the uncertainty of the intensity measurements for both solute and solvent²⁰

$$\delta_{\left[\frac{\mu}{\rho}\right][\rho t]_S}^2 = \left(\frac{\delta^2\left(\frac{I - I_d}{I_0 - I_{d0}}\right)}{\left(\frac{I - I_d}{I_0 - I_{d0}}\right)^2}\right) + \left(\frac{\delta^2\left(\frac{I - I_d}{I_0 - I_{d0}}\right)}{\left(\frac{I - I_d}{I_0 - I_{d0}}\right)^2}\right)_{SV} + \delta^2\left(\frac{t_S}{t_{SV}}\right) \ln^2\left(\frac{I - I_d}{I_0 - I_{d0}}\right)_{SV} + \delta_{I_d}^2\left(\frac{1}{(I - I_d)} - \frac{1}{(I - I_d)_{SV}}\right)^2 + \delta_{I_{d0}}^2\left(\frac{1}{(I_0 - I_{d0})} - \frac{1}{(I_0 - I_{d0})_{SV}}\right)^2 \quad (3)$$

Determination of Path Length $[\rho t]_{sv}$ of the Frozen Solutions Using Attenuation Data. Apart from the solvent,

the other significant background absorbers were the air-path, detector gas (N₂), cryostat gas (He), silicone-like Kapton adhesives, and the window materials (a total of seven layers of Kapton tape were used). The background absorption was modeled using calculated X-ray attenuation data from the FFAST tabulation,^{24,25} and the effective thicknesses of the absorbers traversed by the X-ray beam. Where possible, these thicknesses were measured from the actual experimental geometry. The path lengths were then determined in terms of column density $[\rho t]$ by multiplying the thicknesses of the absorbers by their densities. Table 1 lists the background absorbers, effective thicknesses and integrated column densities $[\rho t]_{av}$. The densities of the background absorbers were taken from the literature.

While the path lengths of most experimental components could be directly measured with sufficiently high accuracy, a fitting procedure was required to determine the path lengths of the solvent when mixed with the solute and of the silicone-like holder adhesives. This was performed using the relation between total attenuation and the attenuations from the various components of the experiment:

$$-\ln(I/I_0)_T = \left[\frac{\mu}{\rho}\right]_{sv} [\rho t]_{sv} + \left[\frac{\mu}{\rho}\right]_{N_2} [\rho t]_{N_2} + \left[\frac{\mu}{\rho}\right]_{Si} [\rho t]_{Si} + \left[\frac{\mu}{\rho}\right]_{air} [\rho t]_{air} + \left[\frac{\mu}{\rho}\right]_{He} [\rho t]_{He} + \left[\frac{\mu}{\rho}\right]_w [\rho t]_w \quad (4)$$

where $[\rho t]$ represent the column density of any of the respective absorbers—solvent (*sv*), air, Kapton windows (*w*) etc. This model isolates the accurate solvent background, its path length and separates the background from the attenuation by the sample (solution). However, the attenuation of the isolated solvent varied from that of the solutions because of path length differences between the frozen solutions in different sample compartments, and the sample quantity. Micrometer measurements suggest variations exist in the lengths of the sample chambers by between 0.1% and 0.35%, and this causes errors in the attenuation measurements which must be removed by determination and calibration of the relative path lengths of the solvent and solute in each chamber.

To determine the path length of the solvent relative to the solutions, we have performed fitting of the attenuations from the solutions in two successive steps: The first step (i) is fitting of the pure solvent (Table 2, no. 2) attenuation using eq 4 to determine the path length $[\rho t]_{Si}$ of the silicone-like matter (i.e., silicone adhesive for 8 layers of Kapton tape), where the path lengths of the other absorbers were constrained to their estimated values. Figure 4 shows the modeling of pure-solvent and determining the path length of the silicone-like parameter in first step of fitting. In the second step (ii), the path lengths $[\rho t]_{sv}$ of the scaled solvents of the two solutions (15 mM and 3 mM) were fitted by constraining the path lengths of the determined

Table 2. Attenuation of Ferrocene and Decamethylferrocene (DmFc) Solution Samples^a

samples	position	mass fraction	spacer	density, ρ	$[\rho t]_{\text{nominal}}$	$\left[\frac{\mu}{\rho}\right][\rho t]$
7.75 keV						
no. 1, Fc(15.26)	top (-4)	0.003633 ($\pm 0.03\%$)	1.4924 \pm 0.0021	0.9513 \pm 0.0052	0.2008	1.9887
no. 2, solvent	middle (0)	–	1.4945 \pm 0.0023	0.9485 \pm 0.0045	0.2005	2.0359
no. 3, Fc(3.07)	bottom (+4)	0.000730 ($\pm 0.03\%$)	1.4962 \pm 0.0021	0.9494 \pm 0.0064	0.2009	2.0534
7.74 keV						
no. 1a, DmFc(15.29)	top (-4)	0.006410 ($\pm 0.06\%$)	1.9742 \pm 0.0017	0.9535 \pm 0.0054	0.2661	2.4974
no. 2a, blank-like	middle (0)	–	1.9783 \pm 0.0018	–	–	1.1458
no. 3a, DmFc(3.06)	bottom (+4)	0.001283 ($\pm 0.3\%$)	1.9810 \pm 0.0020	0.950 \pm 0.012	0.2662	2.5540

^aThe fourth column lists the depths of the chambers determining the path length of the X-ray beam. The densities of the frozen solutions at cryogenic temperatures are listed in the fifth column. The *nominal* column densities of the frozen solutions are listed in the sixth column. The attenuations of the frozen solutions (seventh column) were used to estimate the integrated column densities $[\rho t]_{\text{sv}+\text{bkg}}$ of the solutions. There are significant contributions from background absorption.

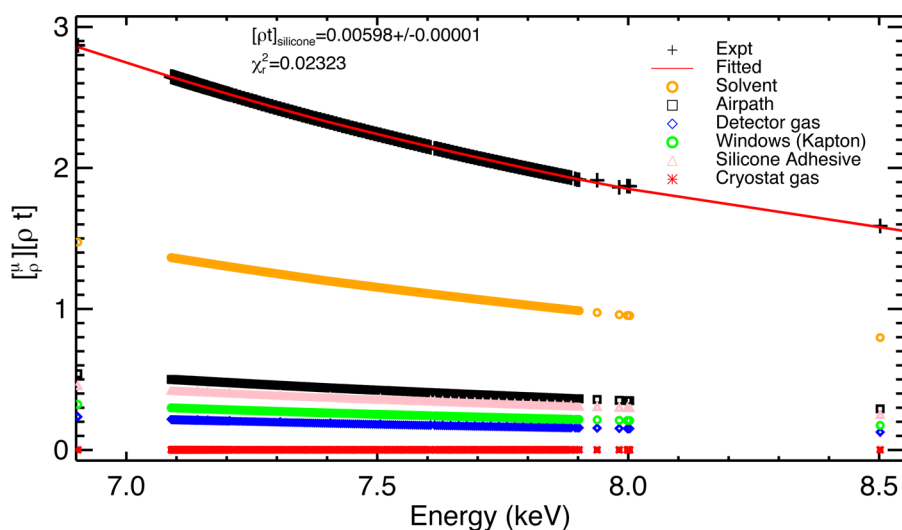


Figure 4. Modeling of the attenuation of the pure solvent and the identified background absorbers. The path length $[\rho t]_{\text{sv}}$ of the silicone-like matter of multiple layers of Kapton tapes was fitted using a model, eq 4, while the path lengths of the other absorbers were constrained to their estimated values. An excellent agreement between theory and experiment provides accurate path lengths $[\rho t]_{\text{sv}}$ of the pure solvent.

silicone-like matter and other background absorbers. The solvent attenuations (baselines) for the mM solutions were scaled by selecting data from the pre-edge and from the postedge (away from the edge). The scaled data were then normalized using their relative masses by multiplying by $\left(1 - \frac{m_s}{m_{sv}}\right)$ to isolate the solvent from the solution, and then fitted to determine the path lengths $[\rho t]_{\text{sv}}$ of the solvents relative to the corresponding solutions. Figure 5 shows the results of this fitting, illustrating the attenuation of the solvent compared with the total attenuation of the solution.

The column-densities $[\rho t]_c$ of the actual material in solutions were determined by multiplying the fitted path lengths $[\rho t]_{\text{sv}}$ by the mass fractions $m_{\text{solute}}/m_{\text{solvent}}$ of the corresponding solutions. Table 3 lists the fitted path lengths $[\rho t]_{\text{sv}}$ of the solutions, and the determined column-densities of the compounds.

Extraction of Attenuation of the Active Species in the Sample. The measured attenuations from the solvent and background structures were subtracted from the total attenuations of the solutions to determine the normalized attenuations $\left[\frac{\mu}{\rho}\right][\rho t]_s$ of the solutes using eq 2. The corresponding uncertainty of the normalized attenuation includes the variance of the repeated measurements with the sample and the solvent (terms 1 and 2 of the RHS of eq 3), absolute uncertainty in

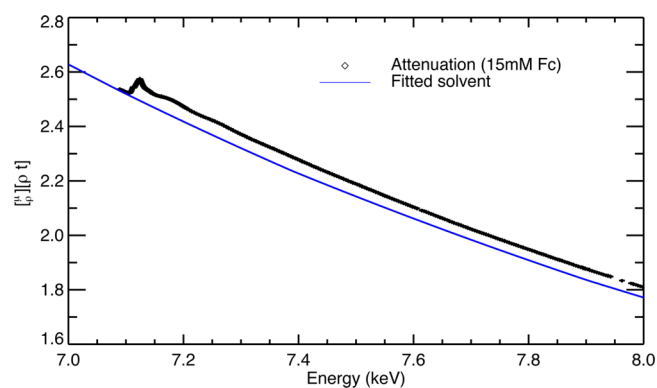


Figure 5. Contribution of the solvent to total attenuation. The blue solid line is the background attenuation determined by fitting the solvent path length using the model given in eq 4. The XAFS of the solute (Fc or DmFc) was then determined by subtracting the solvent background.

determining the path length of the solvent (term 3), and the correlated uncertainty from the dark-current measurements for both solvent and sample measurements (terms 4 and 5). Figure 6 shows the normalized attenuations of Fc from 15 mM (left) and 3 mM (right) solutions. Figure 7 shows the normalized attenuations of DmFc from 15 and 3 mM solutions, together

Table 3. Fitted Path Lengths $[\rho t]$, g/cm^2 , of the Silicone Contact in the pure Solvent Cell, Run 1, Cell No. 2, and Run 2, Cell No. 2a, and Derived Solvent Attenuation in the Solution Cells Nos. 1, 3, 1a, and 3a^a

fitted $[\rho t]$ of silicone = $0.00598 \pm 0.000012 \text{ g}/\text{cm}^2$		
pure solvent (no. 2)		
ferrocene	15 mM Fc (no. 1)	3 mM Fc (no. 3)
$[\rho t]_{\text{fit}} \text{ g}/\text{cm}^2$	0.1836 ± 0.0003	0.20312 ± 0.00024
$[\rho t]_{\text{d}} ([\rho t]_{\text{sv}} \times m_{\text{solute}}/m_{\text{solvent}})$	$0.000667(0.15\%)$	$0.000148(0.12\%)$
$t_{\text{frac}} ([\rho t]_{\text{fit}} / [\rho t]_{\text{nom}})$	0.9158 ± 0.0015	1.013 ± 0.0014
fitted $[\rho t]$ of silicone = $0.01065 \pm 0.00032 \text{ g}/\text{cm}^2$		
blank (no. 2a)		
decamethylferrocene	15 mM DmFc (no. 1a)	3 mM DmFc (no. 3a)
$[\rho t]_{\text{fit}} \text{ g}/\text{cm}^2$	0.24791 ± 0.00041	0.26642 ± 0.00042
$[\rho t]_{\text{d}} ([\rho t]_{\text{sv}} \times m_{\text{solute}}/m_{\text{solvent}})$	$0.00159(0.18\%)$	$0.000342(0.34\%)$
$t_{\text{frac}} ([\rho t]_{\text{fit}} / [\rho t]_{\text{nom}})$	1.0114 ± 0.0023	1.0327 ± 0.0026

^aThe fitted-path lengths of the solutions were then multiplied by the mass-fractions of the respective solutions to determine column-densities for solution attenuation.

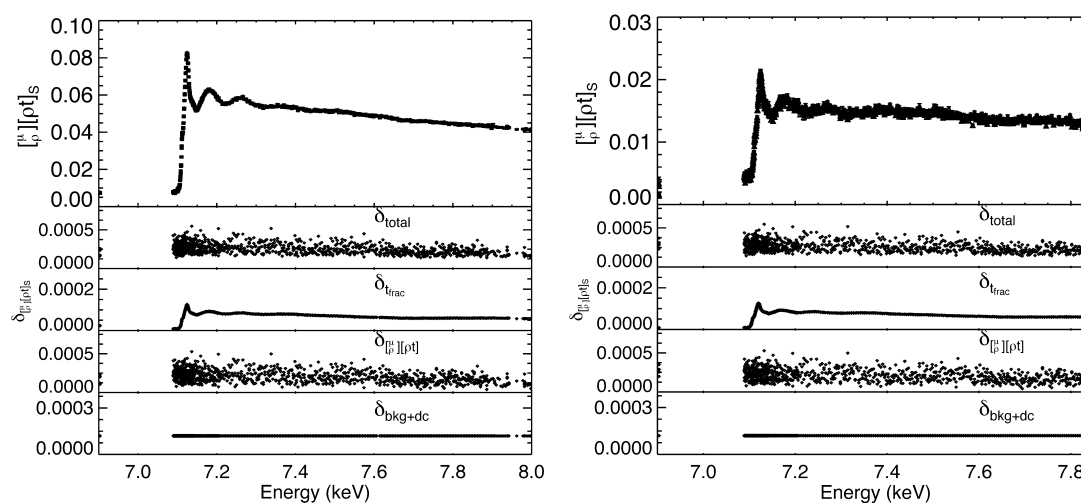


Figure 6. Normalized XAFS of 15 mM Fc (left) and 3 mM Fc (right) with total uncertainties (δ_{total}), uncertainties contributed by solvent path length variation (δ_{trac}), statistical uncertainties ($\delta_{[\rho t]}$), and uncertainties due to background attenuation and dark current ($\delta_{\text{bkg+dc}}$).

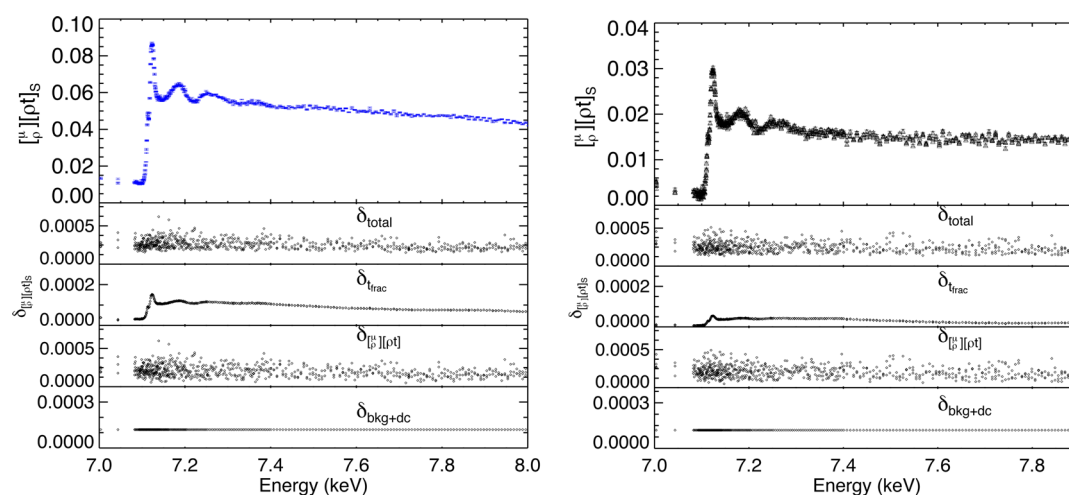


Figure 7. Normalized XAFS of 15 mM DmFc (left) and 3 mM DmFc (right) with total uncertainties (δ_{total}), uncertainties contributed by solvent path length variation (δ_{trac}), statistical uncertainties ($\delta_{[\rho t]}$), and uncertainties due to background attenuation and dark current ($\delta_{\text{bkg+dc}}$).

with uncertainties. The multiple measurements at each of the energies were in excellent agreement for the 15 mM solutions, although weaker with 3 mM solutions with larger relative error,

largely due to statistical variations and background noise, which are expected to be a greater problem for more dilute solutions, which are exaggerated at lower flux beamlines.

5. CHARACTERIZATION OF EXPERIMENTAL SYSTEMATICS FOR THEIR CORRECTION, DEPENDENT UPON BEAMLINE

A number of measurable experimental systematics—energy calibration, photon scattering, and harmonic contamination—were characterized and corrected following the normalization of the attenuations to their solvent backgrounds. These systematics are common to all XAFS measurements and their proper analysis is critical for the level of accuracy sought in this experiment. Since the differences in computed XAFS for different conformers are small, any systematic errors can significantly skew the analysis.

Energy Calibration. The overall hysteresis of the monochromator motor control causes an offset relative to the recorded encoder angle, and therefore an offset in the nominal recorded energy. This is a key experimental systematic and generally applicable to all motor or monochromator systems. Energy calibration is particularly important for the accurate determination of the photoelectron wavenumber k as a function of the calibrated energy.

The BigDiff powder diffractometer was used to measure a number of photon energies across the complete energy range used in this experiment, in order to track both the offset in nominal energy and any drift in this offset. The NIST standard Si(640b) was used—the most accurate powder standard for energy measurements. Figure 8 shows the energy correction to

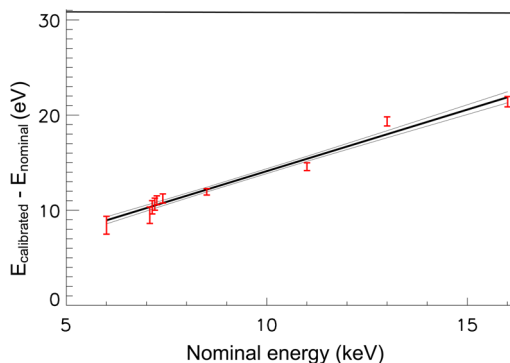


Figure 8. Energy correction to the nominal energy of the X-ray beam using the powder diffraction technique. The measured energies are represented by the red error bars. The black solid line represents the fitted offset, while the thin lines are the 1σ uncertainty envelope. While the offset from the nominal energies was significant, the measurement uncertainties were less than 0.5 eV across the entire range, and down to 0.1 eV in the XAFS region of interest.

the monochromator recorded energies for the measurements with ferrocene. With the same procedure,^{21,26} energy corrections were also made for the measurements with decamethylferrocene (DmFc).

The significant absolute offset in energy (around 10 eV at the Fe K-edge) is important as it affects theoretical analysis of the XANES region, particularly with respect to evaluation of the Fermi level and chemical shifts. Potentially even more significant is the drift in energy, which may cause severe misinterpretations of extended XAFS spectra if uncorrected. The most common problem associated with poor energy calibration is in the determination of bond lengths, while more subtle symmetry, coordination and conformation issues are easily obscured.

Effects of Scattering. To monitor scattered radiation, aperture-dependent measurements were made using three different-sized apertures located on the daisy wheels. In this fashion,

radiation scattered at small angles from the sample and incident on either the upstream or downstream detectors may be progressively filtered in order to assess the level of radiation as a function of the permitted solid angle. In this experiment, however, such an analysis did not find a significant signal corresponding to scattered photons, ergo scattering contributions did not have any material effect on these absorption measurements.

Harmonic Contamination and Correction. When selecting a particular energy of the beam from the monochromator, higher order reflections can contribute harmonic components to the X-ray beam incident on the sample.²² A 0.01–0.2% harmonic contamination was observed at energies from 7.5 keV down to 6.5 keV. Figure 9 shows the attenuation of the beam at 7.16 keV

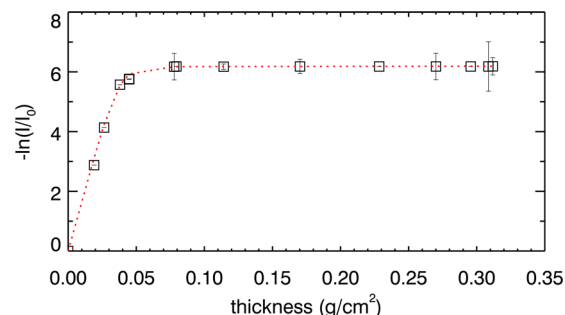


Figure 9. Daisy-wheel measurements of attenuation of a suite of thicknesses of reference foils, measured at a number of energies covering the complete range of attenuation measurements. This plot illustrates the effect of harmonic contamination at 7.16 keV close to the edge. For this energy, the harmonic fraction was measured to be 0.0015(2) (i.e., 0.15%) from the change of linearity from the data points near the knee of the curve.

(close to the Fe K-edge) for different thicknesses of aluminum foils situated on the daisy wheels. The two distinct linear regions represent the dominance of two different X-ray energies, which may be modeled using the expression for monochromated X-ray attenuation in the presence of a single harmonic component:²⁷

$$\exp\left\{-\left[\frac{\mu}{\rho}\right][\rho t]\right\} = (1 - f_n) \exp\left[-\left[\frac{\mu}{\rho}\right]_{E_1} [\rho t]\right] + f_n \exp\left[-\left[\frac{\mu}{\rho}\right]_{E_n} [\rho t]\right] \quad (5)$$

Here E_1 is the primary beam energy, E_n is the energy of the harmonic component, and f_n is the fraction of the harmonic component present in the beam. Tabulations from the FFAST package^{24,25} were used to model the X-ray mass attenuation coefficients $\left[\frac{\mu}{\rho}\right]$ of aluminum at each energy.

A total of five parameters (harmonic fraction— f_n ; attenuation $\left[\frac{\mu}{\rho}\right]_{E_1}$ for fundamental energy E_1 ; attenuation $\left[\frac{\mu}{\rho}\right]_{E_3}$ for the third order energy— E_3 ; a dark current correction; and an offset) were fitted using eq 5 to obtain the harmonic content in the attenuation measurements. The best fit (with lowest χ^2) was obtained by constraining the $\left[\frac{\mu}{\rho}\right]_{E_3}$ parameter to the FFAST tabulated values at higher energies, while leaving it free at lower energies. The effect of the harmonic content on the solution attenuations was then corrected following procedures.^{27,28}

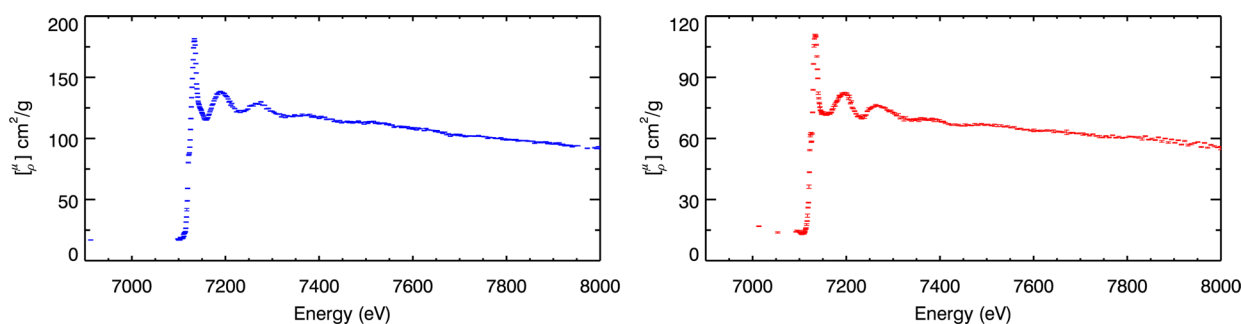


Figure 10. X-ray mass attenuation coefficients $\left[\frac{\mu}{\rho}\right]$ of Fc (left) and DmFc (right) from 15 mM solutions. In the active XANES and in EXAFS regions of Fc XAFS, a 0.3–1% accuracy with a relative precision to 0.1–1% was obtained following the inclusion of uncertainties from systematic corrections. The accuracy of XAFS from 15 mM DmFc was obtained to be 0.4% to 3% with a relative precision to 0.2–2% in the active XANES and EXAFS regions.

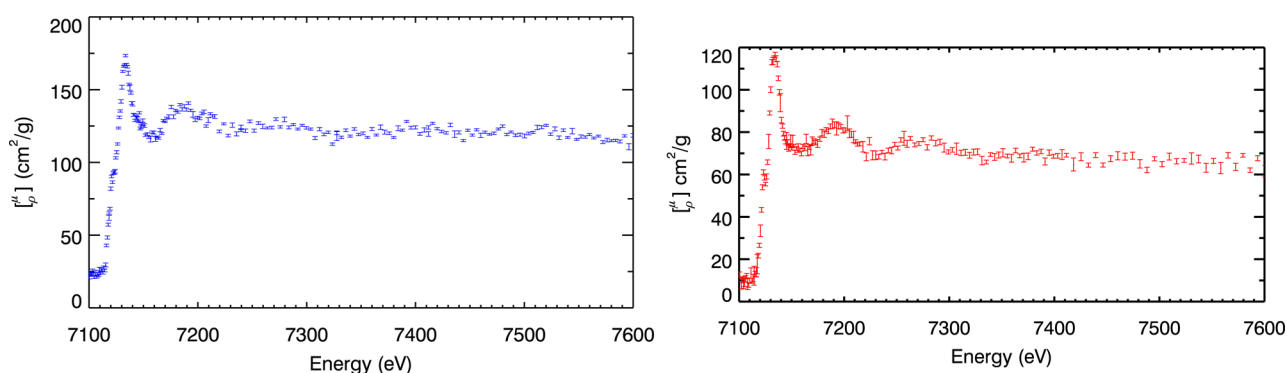


Figure 11. X-ray mass attenuation coefficients $\left[\frac{\mu}{\rho}\right]$ of Fc (left) and DmFc (right) from 3 mM solutions. Structures are well-defined for both Fc and DmFc compounds.

Harmonic effects up to 0.23% at energies up to 7500 eV were observed, while 0.17% harmonic contamination was found at the edge energy 7110.77 eV, but only 0.01% at the lower limit of 6500 eV for these measurements.

6. X-RAY MASS ATTENUATION COEFFICIENTS OF COMPOUNDS FROM DILUTE SOLUTIONS

Accurate determination of integrated column densities $[\rho t]$ of the frozen solutions from the fitting procedure allowed determination of absolute integrated column densities $[\rho t]_S$ of the solutes, corresponding to the Fc and DmFc compounds. The relationship between these parameters simply requires the mass ratio of the solvent and solute (e.g., from Table 2):

$$[\rho t]_S = [\rho t] \frac{\frac{m_S}{m_{SV}}}{1 + \frac{m_S}{m_{SV}}} \quad (6)$$

Normalized and corrected attenuations $\left[\frac{\mu}{\rho}\right][\rho t]_S$ were divided by the column densities to obtain the X-ray mass attenuation coefficients $\left[\frac{\mu}{\rho}\right]$ of the compounds. The corresponding uncertainty was determined by dividing the uncertainty of the normalized XAFS spectra by the fitted path length $[\rho t]_{SV}$ of the pure solvent.

The weighted average of multiple measurements at each of the energies was taken as the final value of the X-ray mass attenuation coefficient $\left[\frac{\mu}{\rho}\right]$:

$$\left[\frac{\mu}{\rho}\right] = \frac{\sum_{\text{all}} \left[\frac{\mu}{\rho}\right]_i / \sigma_{[\mu/\rho]_i}^2}{\sum_{\text{all}} 1 / \sigma_{[\mu/\rho]_i}^2} \quad (7)$$

proportionately weighting the contribution of highly accurate data points. $\left[\frac{\mu}{\rho}\right]_i$ are the measured mass attenuation coefficients at each of the energies (for aperture dependent multiple measurements), and $\sigma_{[\mu/\rho]_i}$ are the corresponding weighted uncertainty. The final uncertainty for the mass attenuation coefficient is then given by

$$\sigma_{[\mu/\rho]} = \sqrt{\frac{\sum_i \left(\frac{([\mu/\rho]_i - [\mu/\rho])}{\sigma_{[\mu/\rho]_i}} \right)^2}{(N-1) \sum_i \frac{1}{\sigma_{[\mu/\rho]_i}^2}} + \left(\frac{\sigma_{[\rho t]_c}}{[\rho t]_c} \right)^2} \quad (8)$$

Measured X-ray mass attenuation coefficients from the 15 mM Fc and DmFc compounds are shown in Figure 10. For the 3 mM solutions, measured X-ray mass attenuation coefficients are shown in Figure 11. Corresponding data for Fc are tabulated in the Appendix in Tables A1 and A2, while DmFc values are given in Tables A3 and A4. Note that the “accuracy” for the measurement of $\left[\frac{\mu}{\rho}\right]$ includes estimation of the absolute normalization, while the relative measurement accuracy relates to the ability to determine structure using conventional XAFS

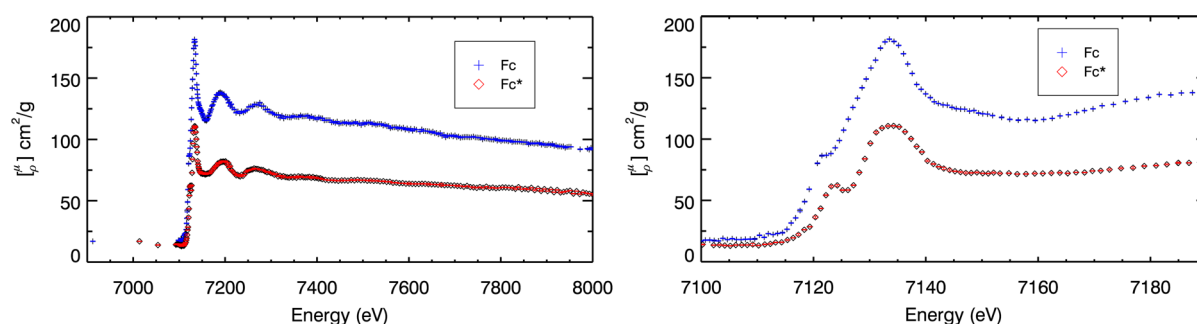


Figure 12. A direct comparison between absolute X-ray absorption spectra of Fc and DmFc (denoted Fc*), without any scaling or background subtraction. The absolute $[\mu/\rho]$ values of Fc are comparatively larger than DmFc, due to a greater percentage of iron in the compound.

modeling and theory, still including most of the systematic uncertainty.

The results from the two different concentrations are broadly consistent for both Fc and DmFc, albeit with a greater noise level in the more dilute 3 mM samples. We also directly compare the XAFS spectra of the two compounds on an absolute scale (Figure 12). There is a small difference in the pre-edge absorption level, and a large difference in the jump-height at threshold between the two compounds, primarily due to the relatively greater concentration of iron in Fc. In terms of spectral structures, the pre-edge peak resulting from the bound–bound 1s–3d transition is more pronounced in the DmFc spectrum, due to a slightly lower Fermi level induced by the local co-ordination environment (i.e., chemical shift). Other features in the XANES region are similar but less pronounced in DmFc, an effect which is due to formal centrosymmetry and perhaps also the relatively disordered influence of the distant methyl structures in the molecule. As the energy increases, the spectral features from Fc and DmFc increasingly resemble one another as the nearest-neighbor carbon rings become increasingly dominant. The detailed tabulations of measurements with uncertainties for the attenuation coefficients and absorption coefficients from the 15 mM solutions and the more dilute solutions are presented in Supporting Information, Tables A1–A4. These are both proofs of accuracy and consistency and also reference spectra for a variety of future investigations, theoretical tests and standards work.

Extraction of Oscillatory Spectral Structures for Conformational Analysis. For most current XAFS analysis techniques, including the FEFF and IFEFFIT packages, Figures 10 and 11 need subtraction of an atomic baseline to isolate their oscillatory components. The oscillatory function, $\chi(k)$, is defined in terms of the total spectrum following

$$\chi(k) = \frac{\mu(k)}{\mu_0(k)} - 1 \quad (9)$$

where $\mu(k)$ is the total photoabsorption of the compound, and $\mu_0(k)$ is a smooth background function approximately corresponding to the absorption of an isolated atom (in this case Fe). The wavenumber of the photoelectron k is related to the energy of the incident photon by

$$k = \sqrt{\frac{2m}{\hbar^2}(E - E_0)} \quad (10)$$

Here m is the electron mass, E the photon energy, and E_0 is the edge position or ionization threshold (7110.77 eV for Fe). Note that in general this is not the same as the Fermi energy, which may vary based on bonding arrangements and affect the presence of bound–bound contributions to the spectrum.

The background function $\mu_0(k)$ has been approximated by a spline approach following an extended implementation of the IFEFFIT package, “IFEFFIT-like”,²⁹ which explicitly includes propagation of experimental uncertainties in the analysis, so the uncertainty of the oscillatory function can be quantified

$$\sigma_\chi = \sigma_{\mu(k)}/\mu_0(k) \quad (11)$$

where $\sigma_{\chi(k)}$ is the uncertainty of $\chi(k)$, and $\sigma_{\mu(k)}$ the uncertainty of the total absorption. The spline approach allows apparent excellent agreement with experimental data and is widespread across the community, but introduces errors and uncertainty due to artificial oscillatory structures.³⁰ Note also that the use of an offset E_0 to define $k = 0$ can vary significantly (and unphysically) for cognate molecules such as Fc and DmFc. Nevertheless, the spline approach is currently the most commonly used approach for the isolation of XAFS oscillatory structure and we follow this standard herein.

As expected, the direct contribution of XAFS to the absorption spectrum takes the form of a rapidly decaying oscillation (Figure 13). The lower plots are of a form commonly used to assess the range of information content accessible by the measurements, but importantly because of our analysis and the propagation of uncertainty, we see precisely the onset and development of statistical and systematic noise and limitations of any data set. Oscillations in the XAFS spectra are well-defined for both Fc and DmFc up to at least $k = 11 \text{ \AA}^{-1}$, with potential for structural analysis within an acceptable noise threshold up to $k = 13\text{--}14.5 \text{ \AA}^{-1}$. The quality of this data is critical for structural analysis of the Fc and DmFc compounds, and in particular for the determination of conformational state. For these materials, different conformers are identifiable with XAFS only in terms of their second-order scattering contributions, which are significant in the XANES region, but across the XAFS region are always dominated by the first-order scattering paths. IFEFFIT and IFEFFIT-like compute data with a constant k spacing—i.e., involving interpolation between points of the actual observed measurements. The plots (Figure 13) show the data used in the analysis.

7. THEORY AND ANALYSIS OF EXPERIMENTAL DATA

Presentation of Prototype Structures from Experiment.

The XAFS spectra measured in the previous sections are among the most highly accurate available for dilute chemical systems. We now implement a range of tests and analyses to discriminate between potential molecular structures and ascertain the conformation states for isolated molecules at temperatures close to absolute zero. Theoretical analysis begins with a comparison of different molecular structures reported for crystalline

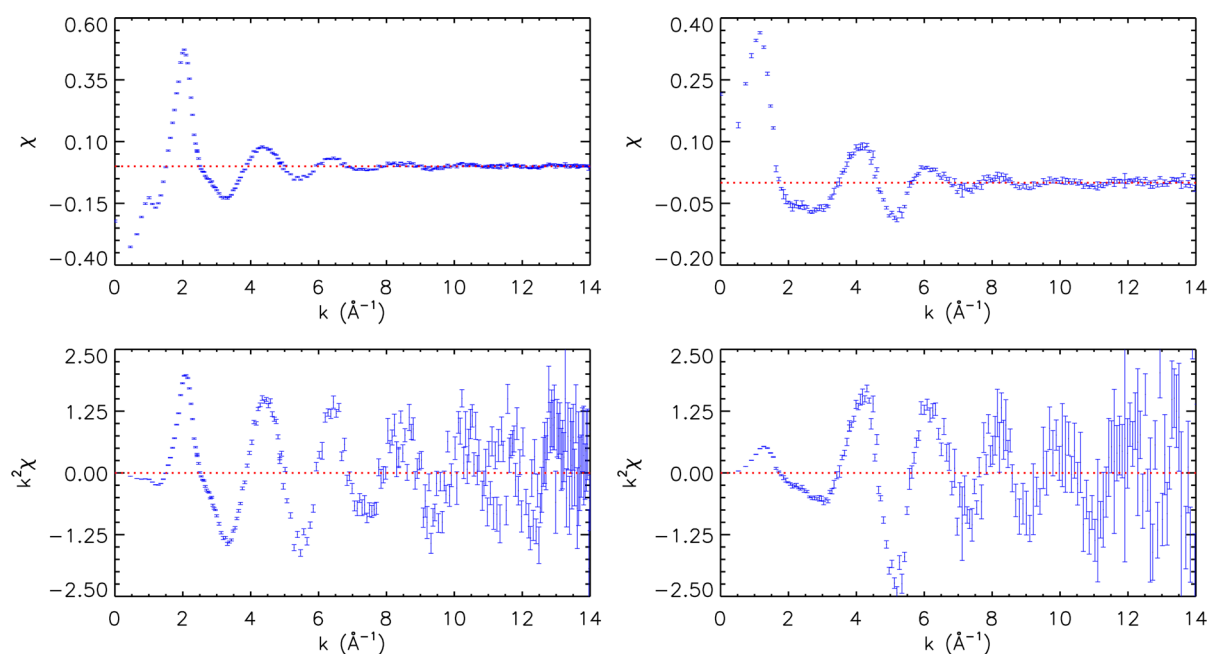


Figure 13. Unweighted and k^2 -weighted transmission XAFS spectra of 15 mM solutions of Fc (left) and DmFc (right) at 10–20 K. Background subtraction using an IFEFFIT splining approach allows the determination of χ vs k plots at the measured energies with the propagation of experimental uncertainties.

Fc and DmFc at different temperatures. Although our measurements should probe a structure closest to that of low-temperature crystals, the absence of crystal packing effects in the solution samples may lead to structural changes. The FEFF package was used to compute XAFS spectra for three reported Fc structures and two reported DmFc structures,³¹ and then apply a refinement algorithm using our “IFEFFIT-like” package²⁹ to evaluate the agreement with our measured spectra. The prototype Fc structures compared in Figure 14 are as follows:

- This structure was determined by Dunitz et al.³² at room temperature (298 K) and reported to have a staggered D_{5d} symmetry with average bond distances of Fe–C = 2.045 ± 0.01 Å and C–C = 1.403 ± 0.02 Å. The crystal packing is monoclinic with $a = 10.561(10)$, $b = 7.597(7)$, and $c = 5.952(6)$ Å; $\alpha = \gamma = 90^\circ$, and $\beta = 121.02^\circ$.
- This structure was determined by Takusagawa et al.¹⁹ at 173 K, and was used by Brock et al.³³ to study the rigid-body disorder models of ferrocene in the high-temperature phase. The crystal packing of this structure is also monoclinic, with cell parameters $a = 10.443(5)$ Å, $b = 7.572(4)$ Å, and $c = 5.824(4)$ Å; $\beta = 120.95(8)^\circ$. Notably, this structure permitted refinement of the hydrogen atoms, which typically make a small contribution in XAFS but may prove significant in the study of such subtle conformational effects.
- This structure is a lower temperature (98 K) Fc structure reported by Seiler et al.³⁴ In this case, an orthorhombic crystal packing is modeled, with cell parameters $a = 6.987(6)$ Å, $b = 8.995(7)$ Å, and $c = 12.196(5)$ Å. Most notably, the cp rings for this structure are closer to eclipsed, with a rotation angle of 9° .

For decamethylferrocene (DmFc) we test two reported structures, both measured using X-ray diffraction at room temperature.^{35,36} These structures were modeled using orthorhombic crystal packings, and both possess staggered geometries for the cp rings. The detailed parameters defining the DmFc structures are given in Table 8, along with refinement parameters using our

experimental data. There are some concerns with these structural determinations and recent work has suggested a different space group;³⁷ however, the structures are illustrative and in any case require refinement for comparison to solution XAFS data.

Analysis and Investigation of Reported Fc Structures.

The structure of Fc is interrogated by a theoretical mapping of the reported experimental structures from the previous section into XAFS spectra using the FEFF8 package,³¹ and subject the outputs to a robust reparameterization using our extension of the popular IFEFFIT package^{6,38} commonly used for XAFS refinement and least-squares fitting.³⁹ In this fashion bond lengths (via an expansion parameter), many-body multiple scattering effects, ionization level, static and thermal disorder may be adjusted for each structure in order to maximize agreement with the experiment data. These refined parameters, along with resulting χ_r^2 values representing goodness of fit, are detailed in Table 4.

Table 4 also provides information regarding the various bond distances and Fe to cp plane distance (Fe–C_s) for each of the reported Fc structures. The refined XAFS parameters are the contribution of shake processes (S_0^2), an expansion parameter scaling bond lengths from their nominal value (α), the fitted effective Debye–Waller factor (σ^2), and the ionization energy offset from its nominal value (E_0). The Debye–Waller factor, typically associated with thermal disorder, is largely a measurement of the static (i.e., structural) disorder in the system due to the small thermal motion at our measurement temperature of 10–20 K.

Influence of the hydrogen atoms reported in the structures from Brock et al. and Seiler et al. are initially excluded to obtain as direct a comparison as possible. In the absence of hydrogen, the χ_r^2 values for the structures differ by small amounts, lower temperature data are improved model functions for the experimental data. This is an important test of consistency between the models from the experiments and of the theoretical mappings.

When the hydrogen atoms are included in the theoretical XAFS determination, the agreement with experiment becomes

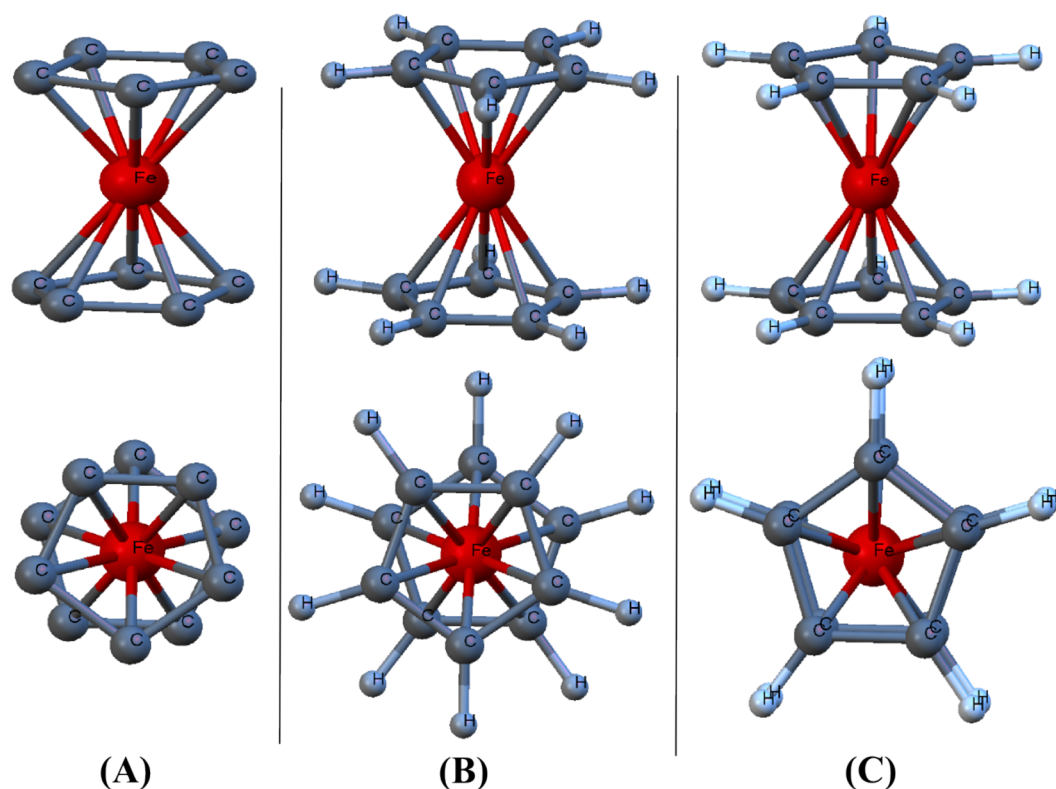


Figure 14. Crystal structures of Fc based on measurements at three different temperatures (283 (part A), 173 (part B), and 98 K (part C)) reported respectively by Dunitz et al.,³² Brock et al.,³³ and Seiler et al.³⁴ and used here as the basis for the model developments and conformation analysis of Fc. The higher temperature structures clearly possess a staggered geometry for the cp rings, while the 98 K measurement suggests a near-eclipsed structure with a relative rotation angle of 9°. We note that the lines between Fe and C in particular are to guide the eye and do not imply direct or σ bonding.

Table 4. XAFS Refinement Parameters Using Three Crystalline Ferrocene Structures^a

	Fc cryst. no. 1 (Dunitz et al., ³² 1956)	Fc cryst. no. 2 (Brock et al., ³³ 1997)	Fc cryst. no. 3 (Seiler et al., ³⁴ 1982)
Bond Length, Å			
Fe–C1/Fe–C1a	2.051/ibid	2.055/ibid	2.051/2.054
Fe–C2/Fe–O2a	2.069/ibid	2.032/ibid	2.063/2.052
Fe–C3/Fe–C3a	2.070/ibid	2.063/ibid	2.055/2.052
Fe–C4/Fe–O4a	2.010/ibid	2.043/ibid	2.063/2.054
Fe–C5/Fe–C5a	2.024/ibid	2.025/ibid	2.051/2.062
Fe–C (average)	2.05(3)	2.044(7)	2.056(2)
Fe–C _s	1.661	1.644	1.658
C–C (average)	1.40(4)	1.388(1)	1.429(2)
C–H (average)	–	1.075(2)	1.080(1)
temperature (K)	283–300	173	98
XAFS Parameters Excluding H Atoms in the XAFS Model			
S ₀ ²	0.913 ± 0.103	0.917 ± 0.105	0.94 ± 0.10
α	1.001 ± 0.004	1.004 ± 0.003	1.002 ± 0.003
σ^2	0.003 ± 0.002	0.003 ± 0.002	0.003 ± 0.002
E ₀	8.87 ± 1.01	8.16 ± 1.04	7.92 ± 1.10
returned χ_r^2	3.760	3.471	3.363
XAFS Parameters Including H Atoms in the XAFS Model			
S ₀ ²	–	1.13 ± 0.13	1.10 ± 0.12
α	–	1.012 ± 0.005	1.008 ± 0.004
σ^2	–	0.005 ± 0.002	0.005 ± 0.002
E ₀	–	11.21 ± 1.14	10.56 ± 1.10
returned χ_r^2	–	3.966	3.991

^aBrock et al. (173 K)³³ with D_{5d} symmetry (Figure 14A); Dunitz³² (at 283–300 K) is a distorted staggered structure (Figure 14B); Seiler et al. (98 K)³⁴ is close to the eclipsed geometry with the two Cp rings rotated 9° from the Fe–C_s axis (Figure 14C). The best fit is provided by the Seiler structure. Inclusion of H atoms introduces a large number of well-defined scattering paths, which do not improve the fits.

Table 5. XAFS Refinement Using Regularized Structures of Crystalline Fc from Measurements by Brock et al. and Seiler et al.^a

	Fc cryst. no. 2 regularized	Fc cryst. no. 3 regularized	Fc cryst. no. 2 regularized and refined bond lengths	Fc cryst. no. 3 regularized and refined bond lengths
Bond Length, Å				
Fe–C (average)	2.044	2.056	2.047(2)	2.055(2)
Fe–C ₅	1.644	1.658	1.652(1)	1.655(1)
C–C (average)	1.388	1.429	1.402(1)	1.433(2)
C–H (average)	1.076	1.080	ibid	1.078(2)
XAFS Parameters: Single Thermal Parameter σ^2 (Å ²) (Including H Atoms in the XAFS Model)				
S ₀ ²	0.98 ± 0.12	0.964 ± 0.116	0.993 ± 0.12	0.94 ± 0.06
α	1.004 ± 0.003	1.001 ± 0.001	1.006 ± 0.004	1.001 ± 0.002
σ^2	0.004 ± 0.002	0.005 ± 0.002	0.004 ± 0.002	0.005 ± 0.001
E ₀	9.98 ± 1.1	9.65 ± 1.06	9.43 ± 1.03	8.14 ± 1.05
returned χ_r^2	3.44	3.28	3.25	3.17
XAFS Parameters: Multiple Thermal Parameter σ^2 (Å ²) (Including H Atoms in the XAFS Model)				
S ₀ ²	0.873 ± 0.039	0.91 ± 0.03	0.97 ± 0.11	0.92 ± 0.05
α	1.002 ± 0.004	1.001 ± 0.001	1.003 ± 0.002	1.002 ± 0.001
σ^2	0.008 ± 0.003	0.007 ± 0.004	0.006 ± 0.003	0.008 ± 0.003
E ₀	9.96 ± 1.01	8.05 ± 0.88	8.06 ± 0.86	7.64 ± 0.76
returned χ_r^2	3.35	3.17	3.16	3.06

^aThe regularization enforces consistent bond distances for Fe–C, C–C, and C–H, Fe–C₅ based on their average values. We separately perform fits using refinements of the key Fe–C bond distance for improved χ_r^2 minimization. Fittings were also performed using both single effective and multiple thermal/disorder parameters.

significantly worse. This is most likely due to a poor quantification of the hydrogen atom positions, which have lower mass and larger positional distribution than the carbon atoms. Indeed, this is directly implied by the increase in the fitted values for σ^2 . It is most probable that the uncertainty of position for the hydrogen atoms due to static disorder is substantially greater than for carbon, and thus their inclusion with a single effective σ^2 is actually a significant source of error when these reported molecular structures are used. For XAFS modeling we have used the maximum effective distance (RPATH keyword in FEFF8 program) to be 4.2 Å, allowing 23 paths, and NLEG equals 6. This ensures the inclusion of the critical paths from multiple scattering which differ between the two conformations.

In a similar vein, the variation between Fe–C bond lengths in the structures reported in Table 4 are in many cases smaller than the fitted level of disorder in the molecule. It is therefore reasonable to define a “regularized” model of the structures, where the cp rings take the form of regular pentagons, with the bond lengths taken as the average bond length from each reported structure. We also investigate two fitting regimes for these regularized structures—one in which a single effective σ^2 value is retained, and one in which separate σ^2 values are taken for the carbon and hydrogen atoms. Refined parameters and χ_r^2 values for these fits are given for the structures provided by Brock et al. (Fc cryst. no. 2) and Seiler et al. (Fc cryst. no. 3) in Table 5. In this table and elsewhere, the value given for the *single thermal parameter* σ^2 is based principally on the disorder of the nearest neighbor carbon atoms, while the value given for the *multiple thermal parameter* σ^2 fit is based on the disorder of the next nearest-neighbors (hydrogens for Fc, and methyl structures for DmFc). In all cases where multiple thermal parameters are used, the value of 0.001 Å² was used for the Fe–C–Fe paths as determined from correlated Debye modeling. The other parameters are presented in the corresponding tables.

A compelling result from these fits is that even when a single effective σ^2 value is retained, the χ_r^2 values are improved for the regularized versions of both structures. This implies that the variation in bond length between the various carbon atoms is

indeed best modeled as a statistical variation from an equilibrium displacement, which manifests here as a higher total Debye–Waller factor. When multiple σ^2 values are used, corresponding to different disorder for the carbon and hydrogen atoms, further reductions are obtained in the χ_r^2 values, leading to better fits than any structures previously tested. Although each of these improvements is incremental, the total improvement from the fits in Table 4 is significant, achieved with full modeling of the Fc molecule inclusive of all neighboring atoms.

Here we also fit the aggregate bond distances Fe–C, C–C, and C–H. The fitted parameters for these regularized *and* refined structures are provided in Table 5 based on the initial structures from Brock et al. and Seiler et al. In both cases, the changes in bond lengths are quite small, but the improvement in agreement with our experimental XAFS spectra is significant. This is a multifactorial effect that comes from both the structural refinement and change of fitted XAFS parameters, particularly the ionization or chemical shift (E_0). As with all previous fits, the best agreement with our data is obtained with the use of a structure based on the low temperature analysis of Seiler et al., which uses an eclipsed geometry for the cp rings.

Conformation Analysis of Fc and Sensitivity of cp Ring Rotation to XAFS. With the regularized and refined geometry based on the measurements of Seiler et al., we are now in a position to quantify the impact of rotations of the cp rings on the agreement with our low temperature experimental data. For this analysis we focus on the structure that has provided the best match thus far, Fc cryst. no. 3 from Table 5, and consider three different conformers as illustrated in Figure 15.

The conformers correspond to (A) an eclipsed structure with rotation angle $\theta = 0^\circ$, (B) a state with $\theta = 18^\circ$, and (C) a staggered structure with the rings offset by $\theta = 36^\circ$. We constrain the positions by regularization of the structure of Seiler et al., defining parallel cp planes with origins equidistant from the central Fe atom.

The difference between conformations in their corresponding XAFS spectra arise from the contributions of the scattering paths which are different for each structure. For Fc, these are only the

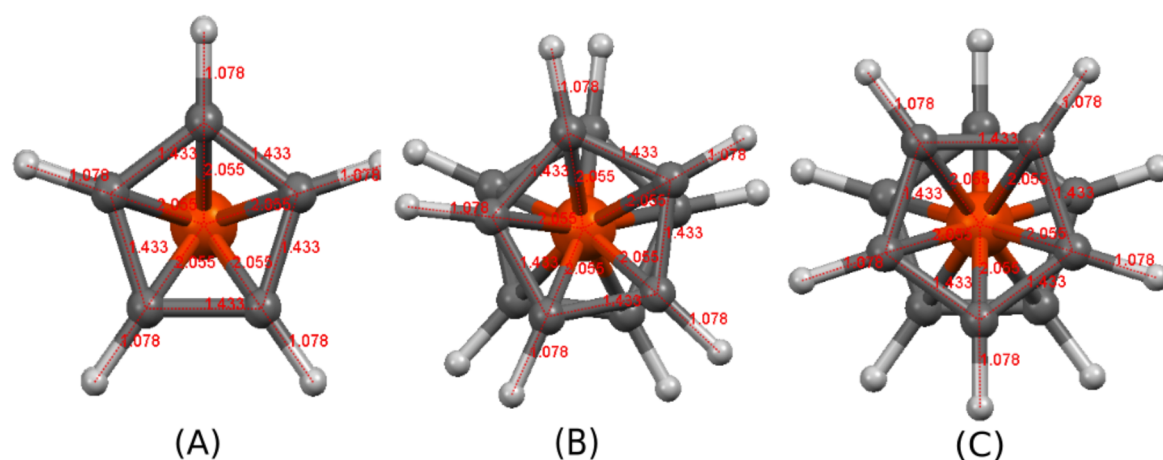


Figure 15. Rotated models using the refined values of the Seiler's crystalline Fc (the fifth column in Table 5). One of the cp rings of the symmetrized eclipsed model D_{5h} (part A) was rotated by 36° to produce a staggered D_{5d} structure (part C), and separately by 18° to produce a mixture state $D_{5d} + D_{5h}$ (part B).

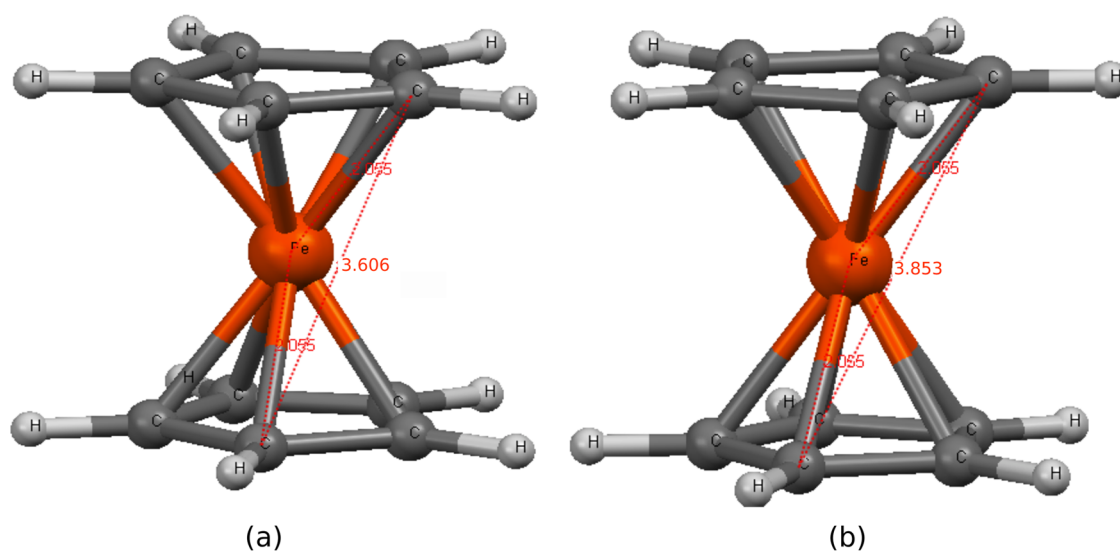


Figure 16. Equivalent multiple scattering paths (Fe–C–C–Fe) probing each cp ring travel different lengths with different multiplicities for the staggered and eclipsed geometries (7.7 Å for eclipsed; 7.9 Å for staggered).

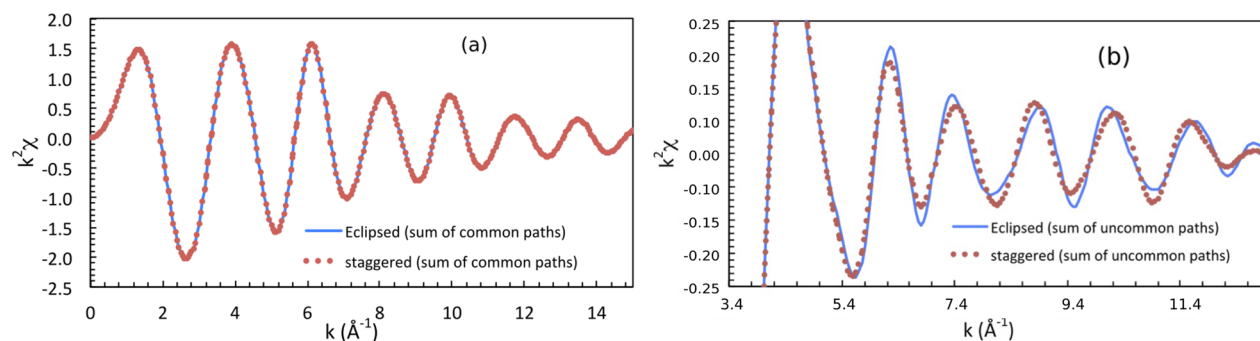


Figure 17. Total XAFS signals from the sum of the common paths, and of the uncommon paths between the staggered and eclipsed conformations. The comparison was made following the refinement of Seiler's model and symmetrizing to be eclipsed, and staggered (by rotating one of the rings by 36°), where the relative bond distances between the conformations were the same shown in Figure 15.

second-order scattering paths that involve reflections from both of the carbon rings before returning to the central iron atom. Examples of such paths are shown in Figure 16.

Although the inequivalent scattering paths have quite similar lengths, resulting in XAFS oscillations of similar frequency, they

can contribute noticeably different amplitudes to the oscillatory part of the spectrum (Figure 17). Further, these differences can be strongly k - or energy-dependent. This is because the second-order scattering paths from the staggered conformer are slightly longer, and are thus typically weaker in amplitude due to wave

Table 6. XAFS and Structural Refinement Parameters from Fits of Refined and Regularized Fc Conformations Varied by Relative Cp Ring Angle Using a Single Effective Debye–Waller Factor σ^2 and Multiple Path-Dependent σ^{2a}

XAFS parameters (Å)	single σ^2 (Å ²)			multiple σ^2 (Å ²)		
	eclipsed (D_{Sh})	$D_{Sd} + D_{Sh}$ (18° rotation)	(D_{Sd}) (36° rotation)	eclipsed (D_{S-h})	$D_{Sd} + D_{Sh}$ (18° rotation)	D_{Sd} (36° rotation)
S_0^2	0.96 ± 0.06	0.89 ± 0.05	1.00 ± 0.08	0.94 ± 0.02	0.97 ± 0.02	0.99 ± 0.07
α	1.001 ± 0.002	1.001 ± 0.003	1.002 ± 0.003	0.999 ± 0.004	1.001 ± 0.003	1.001 ± 0.002
σ^2	0.005 ± 0.001	0.004 ± 0.001	0.006 ± 0.001	0.003 ± 0.002	0.003 ± 0.002	0.004 ± 0.002
E_0	7.68 ± 0.72	7.73 ± 1.03	7.63 ± 0.34	7.34 ± 0.45	7.12 ± 0.37	7.62 ± 0.52
returned χ_r^2	3.08	3.23	3.75	2.98	3.16	3.58

^a χ_r^2 values improve as structures approach the eclipsed geometry, demonstrating consistency with previous sections.

Table 7. Fitted XAFS Parameters Using Structural Models of the Fc Conformations (D_{Sh} and D_{Sd}) Constructed Using DFT Calculations with B3LYP and CCSD(T) Geometry Optimization^a

	B3LYP model		CCSD(T) model	
	eclipsed	staggered	eclipsed	staggered
Fe–C	2.065	2.068	2.056	2.058
C–C	1.428	1.428	1.433	1.432
Fe–C ₅	1.670	1.674	1.655	1.659
C–H	1.082	1.082	1.077	1.077
		Fitted		
χ_r^2	3.46	3.62	3.02	3.66
amp. reduction factor S_0^2	1.00 ± 0.07	0.98 ± 0.08	0.95 ± 0.10	1.00 ± 0.10
expansion coefficient α	1.00	1.00	1.00	1.00
thermal parameter (σ^2)	0.006 ± 0.001	0.005 ± 0.001	0.005 ± 0.001	0.006 ± 0.001
energy offset (ϵ_0)	4.64 ± 0.33	4.95 ± 0.34	3.67 ± 1.07	3.93 ± 0.35

^aEven in the absence of explicit fitting of the structural parameters, the CCSD optimization performs very well, while once again the eclipsed geometries produce consistently better fits to our experimental data.

function dispersion and energy-dependent inelastic scattering. However, these staggered structure inequivalent paths also have twice the degeneracy of the analogous paths for the eclipsed structure, and so at some energies, they can provide a larger oscillatory structure. Figure 17 shows the relative contributions of the common paths for the eclipsed and staggered conformers and separately the contributions from their uncommon paths. The plot shows the difference between the second- and higher-order scattering paths for each conformer, and also demonstrates the level of detail required for an XAFS measurement in order to isolate these signatures and thus differentiate between Fc conformers. The contribution from uncommon paths is roughly an order of magnitude less than the common paths, and the differences between the conformers is a small fraction of that already small contribution. High sample quality and high absolute accuracy of experimental results is required for such discrimination to be made.

Two previous excellent studies have been made on the XAFS of ferrocene, both by outstanding groups. In the first study,⁴⁰ two background subtraction techniques were investigated, one using a Fourier filtering and the other similar to spline removal. The differences in structural determination and bonding were significant, and the limitations of theory were presented. In particular, the paper emphasized that while obtaining reliable structural information was fraught, the technique was potentially quite sensitive to structural and bonding differences. The second study⁴¹ used muffin-tin theory similar to current popular approaches and commented that no useful comparison could be made any more compared to the earlier data because of the data quality. They found no theoretical difference between the conformer XAFS paths and result, and therefore, it was impossible to distinguish the conformers on the basis of XAFS. Our result here demonstrates that, even with muffin-tin potential theory, it is in fact possible to define structures between conformers and ergo to define

differential signatures, especially (or only) if hypothesis testing using defined uncertainty of experimental data is propagated.

The significant and consistent trend of improved agreement continues between the measured XAFS spectrum and the theoretical spectra generated using structures with eclipsed geometries (Table 6). χ_r^2 values from the eclipsed structure improve on the refined regularized structure of Seiler et al. from Table 5 (Fc cryst. no. 3), which possessed a rotation angle of 9°.

8. XAFS REFINEMENT USING STRUCTURAL MODELS FROM DENSITY FUNCTIONAL THEORY (DFT). INSIGHT FROM THE HYBRID TECHNIQUE

This manuscript has so far dealt exclusively with structural models based on previous measurements reported for crystalline Fc, providing a good grounding from observed structures, yet these structures are not expected to be entirely consistent with our measurements. The samples of this experiment were dilute solutions designed to approximate independent molecules, and measured at $T < 20$ K. We must therefore examine the consistency of experimental conclusions derived using isolated molecular structures predicted via density functional theory (DFT) at or near 0 K. We utilize two different models for geometric optimization—B3LYP¹⁶ and CCSD—to derive the lowest-energy structures exhibiting either ideal eclipsed (D_{Sh}) or ideal staggered (D_{Sd}) symmetry. The corresponding XAFS spectra are again evaluated using the FEFF8 package and compared with the measured data. Unlike with the experimental structures, structural parameters such as bond length, expansion coefficient are not refined, as the DFT structures are intended to represent the optimum measured system directly. XAFS parameters S_0^2 , effective σ^2 , and E_0 were all refined as necessary. Table 7 provides the DFT structural parameters and XAFS fitting results.

The χ_r^2 values here are higher than those for the regularized refined model in Table 6. However, the CCSD optimization performs quite well— χ_r^2 is almost on par with the previous best model for an eclipsed geometry. For both optimizations, the eclipsed structure again provides the greatest level of agreement. In the previous section, all distances were free to adjust independently; however, in the DFT comparison the scale of bond lengths is fixed by the theoretical DFT computations, and is in broad agreement with the crystal determinations. In fact, changing the ratio of the Fe–C₅ distance compared with the ring radius or C–C distance changes the overall significance of the discrimination between the staggered and eclipsed conformers. However, in the range of the experimental ratio, and the experimental and theoretical bond-lengths, we have a useful and reasonably significant discrimination toward the eclipsed structure and away from the staggered conformer. The fitted energy offset from the DFT study is of order 4 or 5 eV \pm 0.4–1.1 eV contrasted with that of 7–8 eV \pm 0.5–1.1 eV in the previous refined regularized result. We comment that this E_0 value is in agreement with observation and modeling of the edge and can be seen as an error (or offset) due to the spline function, so is actually a strong support of the result to within 1–2 eV uncertainty.

This consistency, as much as the absolute variation in χ_r^2 values, provides strong evidence that the eclipsed structure is indeed present in solution at low temperature. A further test of the modeling is required to ensure its robustness for correct structural identification of similar compounds. We move now to an analysis of the expanded structure of decamethyl-ferrocene (DmFc).

9. REFINEMENT OF DMFC CONFORMATIONS AND CONSISTENCY TEST WITH FC CONFORMATIONS

The two prototype structures for DmFc that we investigate are given by Struchkov et al.³⁵ and Freyberg et al.³⁶ Both structures possess a staggered geometry, corresponding to the expected structure arising from the mutual repulsion from the CH₃ ions surrounding the cp rings. Table 8 presents the structural para-

Table 8. XAFS Fitting Parameters and χ_r^2 Values Based on Reported Structures of Crystalline Decamethylferrocene (DmFc)^{35,36 a}

	crystal structure no. 1 (Struchkov et al., 1978)	crystal structure no. 2 (Freyberg et al., 1979)
Bond Length, Å		
Fe–C1	2.055	2.063
Fe–C2	2.056	2.075
Fe–C3	2.055	2.154
Fe–C4	2.055	2.106
Fe–C5	2.055	2.056
Fe–C(ave)	2.0551(2)	2.09(2)
C–C(ave), cp ring	1.431(3)	1.42(1)
C–C(ave), (C–CH ₃)	1.520(6)	1.503(6)
Fe–C ₅	1.655	1.709
XAFS Parameters		
S_0^2	1.10 \pm 0.12	1.14 \pm 0.12
α	0.998 \pm 0.004	0.97 \pm 0.005
σ^2	0.003 \pm 0.001	0.003 \pm 0.002
E_0	–5.104 \pm 1.47	–4.649 \pm 1.76
returned χ_r^2	4.87	4.75

^aSimilar agreement is obtained for each of the tested structures, with low σ^2 values implying relatively little disorder in the measured DmFc samples compared with Fc.

eters and refined XAFS parameters for the two DmFc fits to experiment. The FEFF package determining the XAFS structure utilizes an approximated muffin-tin type potential, so is less robust when considering larger organometallic molecules, resulting in larger χ_r^2 values than for the Fc system. Nevertheless, the fit is reasonable, and the structure of Freyberg et al. appears to match our experimental data well. Struchkov et al.³⁵ has a questionable space group, and the two Cp rings are not planar, which is some cause for concern. Recent work³⁷ favors a structure similar to Freyberg et al.,³⁶ and this is consistent with the current analysis.

Again, we extend our treatment for DmFc by regularizing and refining the bond lengths for each structure. We also consider separately the impact of using a single effective thermal parameter, σ^2 , or multiple parameters for different co-ordination shells. The refined bond distances, XAFS parameters, thermal coefficients and goodness-of-fit parameters are given in Table 9.

Unlike with Fc, there is no clear improvement in the DmFc structures from the regularization process. This implies the reasonable conclusion that the position of the C–CH₃ ligands is more precisely represented than was the case with the CH ligands in Fc, and that the average positions are not dynamically the same for each methyl group, even if their average crystallographic position maybe be identical in solution.

These results do not clearly favor either reported structure; we choose the structure of Freyberg et al. (DmFc cryst. no. 2) for conformational analysis. As with the Fc structure from Seiler et al., we consider rotations of the DmFc structure of Freyberg et al. with Cp ring angles of $\theta = 0^\circ$, $\theta = 18^\circ$, and $\theta = 36^\circ$ (Figure 18).

The XAFS spectra corresponding to the three conformers were fitted to our experimental data (Table 10). As before, a model with a single disorder parameter and a model with path-dependent disorder parameters were considered separately.

Table 10 shows that for both disorder models, the staggered geometry provides the best match for decamethyl-ferrocene. These results are not quite as strong as for Fc (which suggested the reverse) but are nonetheless consistent as the rotation angle is changed, and further consistent with the expectation from the literature and from theoretical modeling. Note a systematic discrepancy in $k^2\chi$ versus k for $9 < k < 11 \text{ \AA}^{-1}$ (Figure 19). This will add to the overall χ_r^2 and may be an indication of longer paths including the methyl carbons, where one might expect a complex dynamic structure from the steric hindrance, as opposed to the simple and almost-planar hydrogen arrangement in Fc.

Clearly, FEFF8 and IFFEFIT-like analysis procedures are sufficiently robust to provide results consistent with expectation and with one another. The greatest weakness of this analysis is likely the limited range of k values that could be considered in the XAFS fitting. Figure 19 shows the oscillatory structure of the best models for Fc and DmFc using eclipsed and staggered geometries, along with the fitting ranges in k -space.

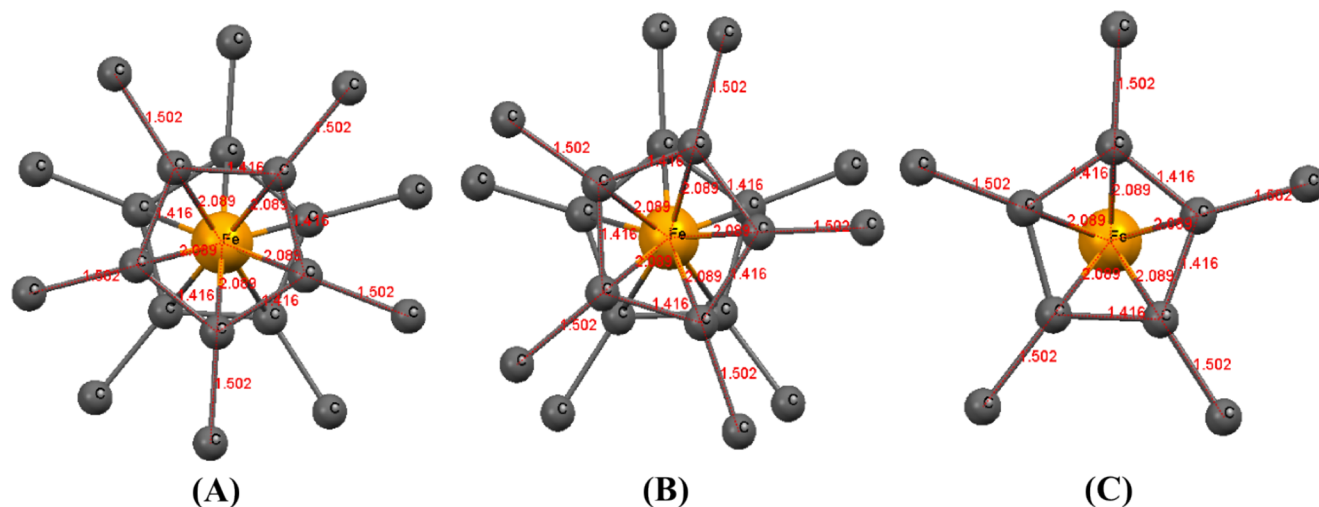
Although we have endeavored to utilize the entire measured range for which there is significant information content, Figure 19 shows that there is substantial disagreement between theory and experiment for k values below 3.5 \AA^{-1} . This has necessarily limited the scope of our analysis, and is an unavoidable consequence of the approximated potential used in full-multiple-scattering XAFS theories. Further investigation is therefore warranted in order to establish the significance of variation between conformers in the low-energy XANES regime, and its impact on the conclusions regarding our refined structures of Fc and DmFc.

The Fc data set has higher noise (up to 3σ) for, e.g., $11 < k < 12 \text{ \AA}^{-1}$ which do not affect the fitting results significantly but

Table 9. XAFS Refinement of the Regularized Structures of Decamethylferrocene Based on the Measurements of Struchkov et al. and Freyberg et al.^{36 a}

	DmFc cryst. no. 1 regularized	DmFc cryst. no. 2 regularized	DmFc cryst. no. 1 regularized and refined bond lengths	DmFc cryst. no. 2 regularized and refined bond lengths
Bond Length, Å				
Fe–C(ave)	2.055	2.09(2)	2.047(2)	2.089(2)
C–C(ave), cp ring	1.431(3)	1.42(1)	1.425(2)	1.416(2)
C–C(ave), (C–CH ₃)	1.520(6)	1.503(6)	1.514(2)	1.502(2)
Fe–C _s	1.655	1.709	1.6494	1.707
XAFS Parameters: Single Thermal Parameter σ^2 (Å ²)				
S_0^2	1.16 ± 0.09	1.13 ± 0.14	1.10 ± 0.08	1.11 ± 0.10
α	0.985 ± 0.005	0.997 ± 0.004	0.997 ± 0.005	0.999 ± 0.006
σ^2	0.003 ± 0.001	0.002 ± 0.002	0.004 ± 0.001	0.003 ± 0.002
E_0	−6.037 ± 1.5	−5.943 ± 2.02	−3.692 ± 1.507	−2.498 ± 1.02
returned χ_r^2	4.82	5.28	4.587	4.329
XAFS Parameters: Multiple Thermal parameter σ^2 (Fe–C–Fe = 0.001 Å ²)				
S_0^2	1.11 ± 0.03	1.10 ± 0.14	1.0 ± 0.1	0.99 ± 0.03
α	0.998 ± 0.004	0.998 ± 0.001	1.001 ± 0.002	1.001 ± 0.003
σ^2	0.004 ± 0.002	0.004 ± 0.003	0.008 ± 0.004	0.007 ± 0.003
E_0	−3.11 ± 1.01	−3.25 ± 1.89	−2.43 ± 0.64	−2.23 ± 0.32
returned χ_r^2	4.62	5.04	4.383	4.154

^aAlso reported are fitting parameters obtained when the average bond lengths are refined, resulting in significantly improved agreement with our own measurements, and a comparison of the results for models using a single or multiple thermal/disorder parameters σ^2 .

**Figure 18.** Conformational views of decamethylferrocene (DmFc) structures used for XAFS modeling. Structure A represents the regularized crystal structure based on the measurement of Freyberg et al.³⁶ at 296 K. Structure B rotates one of the Cp rings by 18° in order to obtain a mixed conformational state, while structure C shows an eclipsed version of the structure.**Table 10.** Refined XAFS Parameters for Fits of DmFc Spectra Based on Regularized Structures from Freyberg et al.³⁵ at Different Angles for the Cp Rings^a

	single σ^2 (Å ²)			multiple σ^2 (Å ²)		
	refined crystal structure-2 (D_{5d})	18° rotation ($D_{5h} + D_{5d}$)	36° rotation (D_{5h})	initial model (D_{5d})	18° rotation ($D_{5h} + D_{5d}$)	36° rotation (D_{5h})
XAFS Parameters						
S_0^2	1.11 ± 0.10	1.11 ± 0.14	1.10 ± 0.04	0.99 ± 0.03	1.03 ± 0.11	0.97 ± 0.10
α	0.999 ± 0.006	1.001 ± 0.002	1.001 ± 0.004	1.001 ± 0.003	1.002 ± 0.003	1.002 ± 0.002
σ^2	0.003 ± 0.002	0.002 ± 0.002	0.003 ± 0.001	0.007 ± 0.003	0.006 ± 0.002	0.007 ± 0.003
E_0	−2.498 ± 1.02	−2.34 ± 1.42	−2.04 ± 0.49	−2.23 ± 0.32	−2.616 ± 1.33	−2.28 ± 0.69
returned χ_r^2	4.33	4.41	4.58	4.15	4.27	4.42

^aIn contrast with the results from Fc, a consistent pattern of improved agreement is seen for structures approaching a staggered geometry.

do yield the overall $\chi_r^2 \approx 3$. Conversely, the DmFc data appears smoother, perhaps up to $k \approx 12.5 \text{ \AA}^{-1}$, but the χ_r^2 over the same window is larger—as a direct consequence of the model deficiency plausibly due to out-of-planar methyl groups. Hence

the uncertainties appear to justify both the dramatically enhanced significance of the data sets and their appropriateness for model testing, while simultaneously presenting explicitly their regions of discrepancy or limitation.

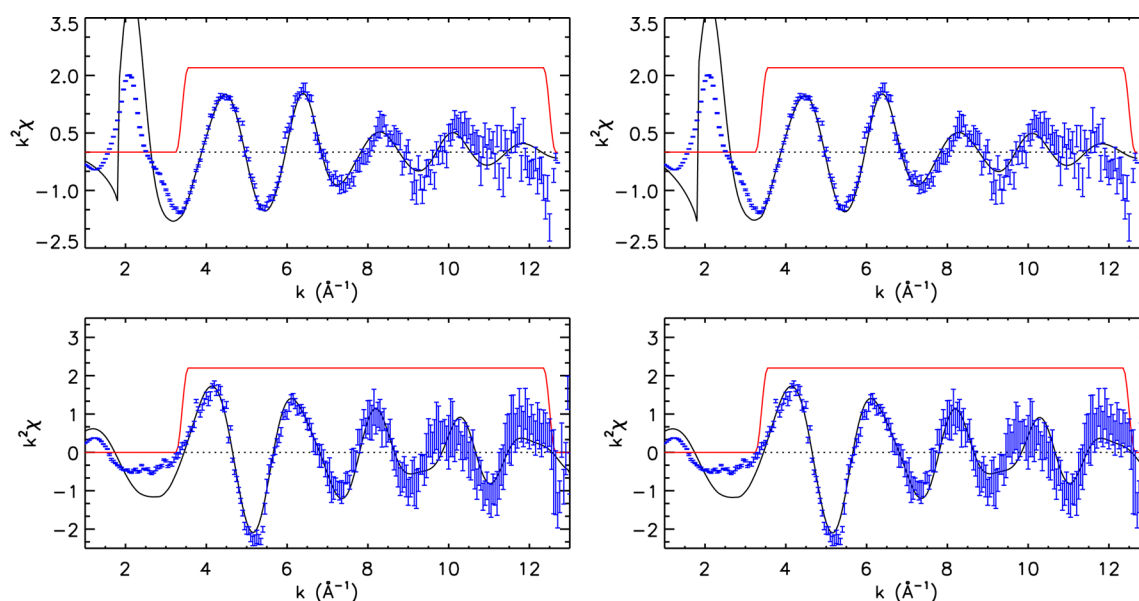


Figure 19. k^2 weighted oscillatory structure from the XAFS spectra of Fc (upper row) using eclipsed (left) and staggered (right) models of the conformational geometry. The lower row shows the same comparison for DmFc. In all cases agreement with experiment is quite good over the fitted k range, but for lower energies the theory and experiment diverge. This enforces a limitation on the scope of the analysis, as the low-energy spectrum tends to be highly sensitive to multiple-scattering contributions.

10. CONCLUSIONS

X-ray absorption spectra including the K-edge and associated fine structure have been measured for frozen dilute samples of the organometallics Fc and DmFc to high absolute accuracy. For Fc, uncertainties for the 15 mM solution in the XAFS region range from 0.3% to 1.0% with a relative precision of 0.14–0.85%, while for the 3 mM solution the uncertainties range from 0.6% to 3.0% with a relative precision of 0.4–2.7%. For DmFc, XAFS from the 15 mM solution was measured to within 0.4–2.5% with a relative precision from 0.2% to 2%, while the 3 mM solution provided accuracies between 0.8% and 5% with a relative precision of 0.7–4.5%.

These measurements have enabled statistically significant resolution of the oscillatory parts of the XAFS spectra up to electron wavenumbers in excess of 12 \AA^{-1} for both materials—a substantially greater range than previously possible using transmission-mode measurements of dilute solutions. This result enables robust and quantitative analysis of a wide range of XAFS phenomena without the ill-defined systematics commonly found in fluorescence measurements such as self-absorption and detector nonlinearity.

We present one of the first high-accuracy XAFS measurements of dilute disordered solutions, and the first for ferrocene Fc and Decamethylferrocene DmFc. To achieve this we use the hybrid technique, measure and propagate uncertainty, both statistical and precision and systematic uncertainties, and use appropriate processing equations to derive the mass attenuation coefficient of the active species and the corresponding derived χ versus k spectra but with uncertainty propagated to permit robust error analysis. It is determined in the present study that the near-eclipsed crystallographic structure determination of Fc by Seiler et al. is closest to our experimental measurement but that the isolated molecule is reflected better by a regularized bipentagon, that thermal factors are very different as expected from the crystal-packed higher temperature forms, and that there is a slight distortion of the bond lengths compared to the crystal structure.

The results have been analyzed with respect to modern full multiple scattering theory and detailed parameter refinement via an extended implementation of the IFEFFIT package. We have found consistent evidence of an eclipsed or near-eclipsed geometry for the isolated low-temperature Fc molecules. These results are consistent with the general agreement from recent high level quantum mechanical studies in the literature; however, there has previously been no direct determination of the conformational structure of such low-temperature Fc in the absence of crystal packing constraints.

Our results are also suggestive of a more regular pentagonal structure for isolated Fc, with random static disorder rather than the distorted structures typically reported for crystalline Fc. This is evidenced by our refinements using regularized versions of experimental structures, and further by the success of the regularized DFT models even in the absence of structural refinements. A modest comparison of alternate DFT model predictions has yielded a consistent estimate for the range of bond-lengths and favors the CCSD(T) modeling environment. Within this, significant evidence is provided for the eclipsed conformer as opposed to the staggered moiety under the experimental conditions. Although the present XAFS measurements are not yet conclusive, they indeed provide further evidence toward the dominance of eclipsed ferrocene conformer in low temperature dilute solutions. All parameters are physical and reasonable in the modeling. Final χ_r^2 values are 3.0, indicative of a very good refinement and a very good enunciation of all error and noise sources, including systematic sources and unknown variance. All results suggest the need for multiple effective thermal parameters, though not strongly so. Regarding DmFc, the distribution of methyl groups is likely to be nonplanar and nonuniform due to steric effects. At this point a staggered structure is preferred by the analysis.

This work represents a powerful demonstration of the utility of XAFS as a structural probe, even for dilute systems and even for quite subtle conformational changes, such as that from the ideal eclipsed to the ideal staggered geometries. Without propagation

of a valid error field, the significance of discriminants between hypotheses is generally arbitrary and guided by eye rather than by the data set. The observation of increasing relative uncertainty at high k provides a natural selection of an appropriate Hanning window for XAFS fitting which would otherwise be arbitrary. Further enhancements of the theoretical and analytical techniques presented are likely to strengthen the outcomes of this investigation, and facilitate yet greater insight into the detailed structural properties of these key organometallic compounds. Furthermore, these approaches apply generally to any metal-centered molecules, crystalline or disordered, in transmission and for dilutions down to 1 mM or better on appropriately optimized beamlines and with significant information content for fitting out to beyond $k > 13 \text{ \AA}^{-1}$.

■ ASSOCIATED CONTENT

● Supporting Information

The Supporting Information is available free of charge on the ACS Publications website at DOI: 10.1021/acs.jpcc.6b00452.

Detailed tabulations of measurements with uncertainties for the attenuation coefficients and absorption coefficients from the 15 mM solutions and the more dilute solutions: Table A1, measured X-ray mass attenuation coefficients $\left[\frac{\mu}{\rho}\right]_S$ of ferrocene (Fc) from the absolute intensities (I_0 and I) for a 15 mM Fc solution; Table A2, measured X-ray mass attenuation coefficients $\left[\frac{\mu}{\rho}\right]_S$ of Fc obtained from the absolute intensities for a 3 mM Fc solution, and its corresponding solvent; Table A3, measured X-ray mass attenuation coefficients $\left[\frac{\mu}{\rho}\right]_S$ of decamethylferrocene (DmFc) using absolute intensities (I_0 and I) for a 15 mM DmFc solution and its corresponding solvent; Table A4, measured X-ray mass attenuation coefficients $\left[\frac{\mu}{\rho}\right]_S$ of DmFc from the intensity measurements (I_0 and I) for a 3 mM DmFc solution and its corresponding solvent (PDF)

■ AUTHOR INFORMATION

Corresponding Author

*(C.T.C.) E-mail: chantler@unimelb.edu.au.

Notes

The authors declare no competing financial interest.

■ ACKNOWLEDGMENTS

We acknowledge the Australian Research Council (ARC) and the science faculty of the University of Melbourne for funding this work. The authors would like to thank the staff of the Australian National Beamline Facility (ANBF), Tsukuba, Japan, where the experiment was performed for their assistance in this work. As the ANBF is now closed, we dedicate this work to the efforts of the Australian and Japanese scientists who have worked together to make the beamline and collaboration such a success.

■ REFERENCES

- (1) Seeman, J. I.; Cantrill, S. Wrong but seminal. *Nat. Chem.* **2016**, *8*, 193–200.
- (2) Ascone, I.; Strange, R. Biological X-ray absorption spectroscopy and metalloproteomics. *J. Synchrotron Radiat.* **2009**, *16*, 413–442.

- (3) O'Day, P.; Rehr, J.; Zabinsky, S.; Brown, G. J. Extended X-ray absorption fine structure (EXAFS) analysis of disorder and multiple-scattering in complex crystalline solids. *J. Am. Chem. Soc.* **1994**, *116*, 2938–2949.

- (4) Wilson, K. R.; Tobin, J. G.; Ankudinov, A.; Rehr, J.; Saykally, R. Extended x-ray absorption fine structure from hydrogen atoms in water. *Phys. Rev. Lett.* **2000**, *85*, 4289.

- (5) Vila, F.; Rehr, J.; Kas, J.; Nuzzo, R.; Frenkel, A. Dynamic structure in supported Pt nanoclusters: Real-time density functional theory and x-ray spectroscopy simulations. *Phys. Rev. B: Condens. Matter Mater. Phys.* **2008**, *78*, 121404.

- (6) Islam, M. T.; Chantler, C. T.; Cheah, M. H.; Tantau, L. J.; Tran, C. Q.; Best, S. P. Structural investigation of mM Ni(II) complex isomers using transmission XAFS: the significance of model development. *J. Synchrotron Radiat.* **2015**, *22*, 1475.

- (7) Newville, M. EXAFS analysis using FEFF and FEFFIT. *J. Synchrotron Radiat.* **2001**, *8*, 96–100.

- (8) Chantler, C. T. Development and applications of accurate measurement of X-ray absorption: The X-ray extended range technique for high accuracy absolute XAFS by transmission and fluorescence. *Eur. Phys. J.: Spec. Top.* **2009**, *169*, 147–153.

- (9) Tantau, L.; Chantler, C.; Bourke, J.; Islam, M.; Payne, A.; Rae, N.; Tran, C. Structure determination from XAFS using high-accuracy measurements of x-ray mass attenuation coefficients of silver, 11 keV - 28 keV, and development of an all-energies approach to local dynamical analysis of bond length, revealing variation of effective thermal contributions across the XAFS spectrum. *J. Phys.: Condens. Matter* **2015**, *27*, 266301.

- (10) de Jonge, M. D.; Tran, C. Q.; Chantler, C. T.; Barnea, Z.; Dhal, B. B.; Cookson, D. J.; Lee, W. K.; Mashayekhi, A. Measurement of the x-ray mass attenuation coefficient and determination of the imaginary component of the atomic form-factor of molybdenum over the 13.5 - 41.5-keV energy range. *Phys. Rev. A: At., Mol., Opt. Phys.* **2005**, *71*, 032702.

- (11) Chantler, C. T.; Islam, M. T.; Best, S. P.; Tantau, L. J.; Tran, C. Q.; Cheah, M.; Payne, A. High-accuracy X-ray absorption spectra from mM solutions of nickel (II) complexes with multiple solutions using transmission XAS. *J. Synchrotron Radiat.* **2015**, *22*, 1008.

- (12) Kealy, T.; Pauson, P. A new type of organo-iron compound. *Nature* **1951**, *168*, 1039–1040.

- (13) Seiler, P. t.; Dunitz, J. The structure of triclinic ferrocene at 101, 123 and 148 K. *Acta Crystallogr., Sect. B: Struct. Crystallogr. Cryst. Chem.* **1979**, *35*, 2020–2032.

- (14) Latouche, C.; Palazzetti, F.; Skouteris, D.; Barone, V. High-accuracy vibrational computations for transition-metal complexes including anharmonic corrections: ferrocene, ruthenocene, and osmocene as test cases. *J. Chem. Theory Comput.* **2014**, *10*, 4565–4573.

- (15) Lippincott, E. R.; Nelson, R. D. The vibrational spectra and structure of ferrocene and ruthenocene. *Spectrochim. Acta* **1958**, *10*, 307–329.

- (16) Mohammadi, N.; Ganesan, A.; Chantler, C. T.; Wang, F. Differentiation of ferrocene D 5d and D 5h conformers using IR spectroscopy. *J. Organomet. Chem.* **2012**, *713*, 51–59.

- (17) Edwards, J.; Kington, G.; Mason, R. The thermodynamic properties of ferrocene. Part 1. The low-temperature transition in ferrocene crystals. *Trans. Faraday Soc.* **1960**, *56*, 660–667.

- (18) Seiler, P.; Dunitz, J. D. A new interpretation of the disordered crystal structure of ferrocene. *Acta Crystallogr., Sect. B: Struct. Crystallogr. Cryst. Chem.* **1979**, *35*, 1068–1074.

- (19) Takusagawa, F.; Koetzle, T. F. A neutron diffraction study of the crystal structure of ferrocene. *Acta Crystallogr., Sect. B: Struct. Crystallogr. Cryst. Chem.* **1979**, *35*, 1074–1081.

- (20) Chantler, C. T.; Islam, M. T.; Best, S. P.; Tantau, L. J.; Tran, C. Q.; Cheah, M. H.; Payne, A. T. High accuracy X-ray absorption spectra from mM solutions of nickel(II) complexes with multiple solutions using transmission XAS. *J. Synchrotron Radiat.* **2015**, *22*, 1008.

- (21) Tantau, L. J.; Chantler, C. T.; Payne, A. T.; Islam, M. T.; Tran, C. Q.; Best, S. P.; Cheah, M. H. High-accuracy X-ray energy determination

and comparison from LaB6 powder diffraction pattern for synchrotron XAFS and XRD calibration. *Radiat. Phys. Chem.* **2014**, *95*, 73–77.

(22) Barnea, Z.; Mohyla, J. Detection of contribution of harmonics to diffracted x-ray intensity. *J. Appl. Crystallogr.* **1974**, *7*, 298–299.

(23) Islam, M. T.; Tantau, L. J.; Rae, N. A.; Barnea, Z.; Tran, C. Q.; Chantler, C. T. Measurement of the X-ray mass attenuation coefficients of silver in the 5–20 keV range. *J. Synchrotron Radiat.* **2014**, *21*, 413–423.

(24) Chantler, C. T. Theoretical form factor, attenuation and scattering tabulation for $Z = 1–92$ from $E = 1–10$ eV to $E = 0.4–1.0$ MeV. *J. Phys. Chem. Ref. Data* **1995**, *24*, 71–82.

(25) Chantler, C. T. Detailed new tabulation of atomic form factors and attenuation coefficients in the near-edge soft X-ray regime ($Z = 30–36$, $Z = 60–89$, $E = 0.1$ keV–8 keV), addressing convergence issues of earlier work. *J. Phys. Chem. Ref. Data* **2000**, *29*, 597–1048.

(26) Rae, N. A.; Chantler, C. T.; Tran, C. Q.; Barnea, Z. Accurate determination of X-ray energies using powder diffraction. *Radiat. Phys. Chem.* **2006**, *75*, 2063–2066.

(27) Tran, C. Q.; Barnea, Z.; de Jonge, M. D.; Dhal, B. B.; Paterson, D.; Cookson, D. J.; Chantler, C. T. Quantitative determination of major systematics in synchrotron x-ray experiments: seeing through harmonic components. *X-Ray Spectrom.* **2003**, *32*, 69–74.

(28) Glover, J. L.; Chantler, C. T.; Barnea, Z.; Rae, N. A.; Tran, C. Q. Measurement of the x-ray mass-attenuation coefficients of gold, derived quantities between 14 and 21 keV and determination of the bond lengths of gold. *J. Phys. B: At., Mol. Opt. Phys.* **2010**, *43*, 085001.

(29) Smale, L. F.; Chantler, C. T.; de Jonge, M. D.; Barnea, Z.; Tran, C. Q. Analysis of X-ray absorption fine structure using absolute X-ray mass attenuation coefficients: Application to molybdenum. *Radiat. Phys. Chem.* **2006**, *75*, 1559–1563.

(30) Tantau, L. J.; Chantler, C. T.; Bourke, J. D.; Islam, M. T.; Payne, A. T.; Rae, N. A.; Tran, C. Q. Structure determination from XAFS using high-accuracy measurements of x-ray mass attenuation coefficients of silver, 11 keV–28 keV, and development of an all-energies approach to local dynamical analysis of bond length, revealing variation of effective thermal contributions across the XAFS spectrum. *J. Phys.: Condens. Matter* **2015**, *27*, 266301–17.

(31) Ankudinov, A.; Rehr, J. Theory of solid-state contributions to the X-ray elastic scattering amplitude. *Phys. Rev. B: Condens. Matter Mater. Phys.* **2000**, *62*, 2437.

(32) Dunitz, J.; Orgel, L.; Rich, A. The crystal structure of ferrocene. *Acta Crystallogr.* **1956**, *9*, 373–375.

(33) Brock, C. P.; Fu, Y. Rigid-body disorder models for the high-temperature phase of ferrocene. *Acta Crystallogr., Sect. B: Struct. Sci.* **1997**, *53*, 928–938.

(34) Seiler, P.; Dunitz, J. Low-temperature crystallization of orthorhombic ferrocene: structure analysis at 98 K. *Acta Crystallogr., Sect. B: Struct. Crystallogr. Cryst. Chem.* **1982**, *38*, 1741–1745.

(35) Struchkov, Y. T.; Andrianov, V.; Sal'Nikova, T.; Lyatifov, I.; Materikova, R. Crystal and molecular structures of two polymethylferrocenes: sym-octamethylferrocene and decamethylferrocene. *J. Organomet. Chem.* **1978**, *145*, 213–223.

(36) Freyberg, D. P.; Robbins, J. L.; Raymond, K. N.; Smart, J. C. Crystal and molecular structures of decamethylmanganocene and decamethylferrocene. Static Jahn-Teller distortion in a metallocene. *J. Am. Chem. Soc.* **1979**, *101*, 892–897.

(37) Makal, A. M.; Plazuk, D.; Zakrzewski, B.; Misterkiewicz, B.; Wozniak, K. Experimental charge density analysis of symmetrically substituted ferrocene derivatives. *Inorg. Chem.* **2010**, *49*, 4046–4059.

(38) Chantler, C. T.; Rae, N. A.; Islam, M. T.; Best, S. P.; Yeo, J.; Smale, L. F.; Hester, J.; Mohammadi, N.; Wang, F. Stereochemical analysis of ferrocene and the uncertainty of fluorescence XAFS data. *J. Synchrotron Radiat.* **2012**, *19*, 145–158.

(39) Newville, M. IFEFFIT: interactive XAFS analysis and FEFF fitting. *J. Synchrotron Radiat.* **2001**, *8*, 322–324.

(40) Cramer, S. P.; Eccles, T. K.; Kutzler, F.; Hodgson, K. O.; Doniach, S. Applications of x-ray photoabsorption spectroscopy to the determination of local structure in organometallic compounds. *J. Am. Chem. Soc.* **1976**, *98*, 8059–8069.

(41) Ruiz-Lopez, M. F.; Loos, M.; Goulon, J.; Benfatto, M.; Natoli, C. R. Reinvestigation of the EXAFS and XANES spectra of ferrocene and nickelocene in the framework of the multiple scattering theory. *Chem. Phys.* **1988**, *121*, 419–437.